INTEGRATION OF GEOMETRY AND ANALYSIS FOR THE STUDY OF LIQUID SLOSHING IN RAILROAD VEHICLE DYNAMICS

Huailong Shi[1] (huai.long.shi@gmail.com)
Liang Wang[2] (liang.wang@mscsoftware.com)
Brynne Nicolsen[2] (bnicols2@uic.edu)
Ahmed A. Shabana[2] (shabana@uic.edu)

[1] State Key Laboratory of Traction Power, Southwest Jiaotong University, Chengdu, Sichuan, China, 610031.
[2] Department of Mechanical Engineering, University of Illinois at Chicago, Chicago, Illinois, USA, 60607.

ABSTRACT

A new continuum-based liquid sloshing approach that accounts for the effect of complex fluid and tank-car geometry on railroad vehicle dynamics is developed in this investigation. A unified geometry/analysis mesh is used from the outset to examine the effect of liquid sloshing on railroad vehicle dynamics during curve negotiation and during the application of electronically controlled pneumatic (ECP) brakes that produce braking forces uniformly and simultaneously across all cars. Using a non-modal approach, the geometry of the tank-car and fluid is accurately defined, a continuum-based fluid constitutive model is employed, and a fluid-tank contact algorithm is developed. The liquid sloshing model is integrated with a three-dimensional multibody system (MBS) railroad vehicle algorithm which accounts for the nonlinear wheel/rail contact. The three-dimensional wheel/rail contact force formulation used in this study accounts for the longitudinal, lateral, and spin creep forces that influence the vehicle stability. In order to examine the effect of the liquid sloshing on the railroad vehicle dynamics during curve negotiation, a general and precise definition of the outward inertia force is defined, and in order to correctly capture the fluid and tank-car geometry, the *absolute nodal coordinate formulation* (ANCF) is used. The balance speed and centrifugal effects in the case of tank-car partially filled with liquid are studied and compared with the equivalent rigid body model in curve negotiation and braking scenarios. In particular, the results obtained in the case of the ECP brake application of two freight car model are compared with the results obtained when using conventional braking. The traction analysis shows that liquid sloshing has a significant effect on the load distribution between the front and rear trucks. A larger coupler force develops when using conventional braking compared with ECP braking, and the liquid sloshing contributes to amplifying the coupler force in the ECP braking case compared to the equivalent rigid body model which does not capture the fluid nonlinear inertia effects. Furthermore, the results obtained in this study show that liquid sloshing can exacerbate the unbalance effects when the rail vehicle negotiates a curve at a velocity higher than the balance speed.

Keywords: Railroad vehicle dynamics; liquid sloshing; centrifugal forces; absolute nodal coordinate formulation.

1. INTRODUCTION

Sloshing is the motion of liquid in a container subjected to forced oscillations and usually occurs in a moving container which is not fully filled. Strictly speaking, the liquid must have a free surface to constitute a sloshing dynamics problem [15]. The highly nonlinear dynamics of the liquid motion can interact with the container to alter the system dynamics significantly. The initial studies on the sloshing effect were for aerospace and ocean science focused on the design and development of high-speed aircraft and large shipping vessels, respectively [1, 9, 11]. However, the high demand of crude oil and other hazardous material (HAZMAT) transportation has resulted in many serious and environmentally-damaging highway and railroad accidents [13, 35]. In railroad transportation, liquid sloshing can have a significant effect on railroad vehicle dynamics, especially in curve negotiation and traction and braking scenarios [30, 31]. Although statistics show that most of the accidents were caused by misuse or careless driving by the operator, extensive mathematical and empirical studies must be performed to examine the effect of liquid sloshing on vehicle dynamics and stability.

In liquid sloshing problems, the main focus is on the nominal fluid motion and its effect on the vehicle dynamics. Therefore, the effect of turbulence is assumed negligible and is not considered in most sloshing investigations. For this reason, simple liquid sloshing models that are based on rigid body assumptions are often used. Simplified equivalent models with discrete inertia and elasticity properties, such as the mechanical-pendulum analogy and equivalent mass-spring systems, were initially introduced to study liquid sloshing problems [10, 20, 21, 30].

Later, energy dissipation was taken into consideration by including dashpots in the sloshing models. However, comparison with computational fluid dynamics (CFD) simulations has shown that these simplified models are not able to accurately represent the system parameters, capture the effect of the distributed inertia and elasticity, or model the shape of the free surface [4, 6, 14]. Modern analysis methods for liquid sloshing typically use CFD algorithms and finite volume and boundary element methods [5, 30]. However, the integration of the Eulerian-based liquid sloshing models with the computational Lagrangian-based MBS vehicle algorithms is difficult because of the fundamental differences between the two approaches. Additionally, use of other particle-based methods such as smoothed particle hydrodynamics (SPH) liquid sloshing models can be computationally very costly [8, 22]. In order to address this concern, a lower order model based on the *floating frame of reference* (FFR) formulation was proposed [31]. While such a continuum-based approach results in a significant computational cost reduction, it has some limitations in the case of large displacement and complex geometry liquid sloshing problems.

In the case of liquid sloshing problems, accurate definition of the geometry of the fluid and container is necessary in order to develop a general computational framework that can be effectively used to shed light on the effect of sloshing in complex motion scenarios. Existing finite element (FE) and modal-based approaches are not suited for accurately representing the geometry and/or capturing the large displacements and spinning motion that characterize railroad vehicle systems. Such FE and modal-based approaches are not compatible with the more accurate computational geometry methods such as B-spline and NURBS (**N**on-**U**niform **R**ational

B-Spline) representations [18]. This is evident by the fact that there is no linear mapping between existing FE displacement fields and B-spline and NURBS geometry. The FE absolute nodal coordinate formulation (ANCF), on the other hand, has one-to-one mapping with B-spline and NURBS geometry, and therefore, ANCF elements can be used to develop a unified geometry/analysis mesh from the outset for the liquid and tank as well as for the rigid track. Furthermore, ANCF elements, which have a constant mass matrix and can be systematically implemented in Lagrangian-based MBS algorithms [33], allow for arbitrarily large displacements, and therefore, can be effectively and efficiently used in modeling liquid sloshing in highly nonlinear scenarios including curve negotiation and sudden braking application.

In the case of sudden braking, severe sloshing forces can be generated, leading to excessive coupler forces between the railcars. The purpose of the newly introduced electronically controlled pneumatic (ECP) braking system, recommended for long freight trains, is to apply the braking forces uniformly and simultaneously on all railcars. Such a new technology can improve both train safety and operations by reducing the coupler forces and decreasing stopping distances. Studies showed that the ECP braking system, as compared to the conventional braking, leads to a 40% reduction in the stopping distance and significant reduction in the coupler forces [2]. However, most investigations on the long train braking use simple vehicle and wheel/rail interaction force models. Additionally, there are no comprehensive studies on the effect of liquid sloshing on rail vehicle dynamics and inter-car forces during train tractions and sudden brake applications.

In this investigation, a computational continuum-based total Lagrangian approach is used to study the effect of liquid sloshing on railroad vehicle dynamics during curve negotiation and braking scenarios. A unified geometry/analysis mesh [7, 26] is used from the outset to define the tank-car and fluid configuration, demonstrating a successful **i**ntegration of **c**omputer **a**ided-**d**esign and **a**nalysis (I-CAD-A) for an important and practical problem. The general definition of the liquid outward inertia forces, which is fundamentally different from the case of rigid body dynamics, is defined in Section 2 of this paper, and it is shown that the conventional centrifugal force definition used to define the vehicle balance speed during curve negotiations is a special case of the more general expression. The geometry description of both the tank and the fluid using ANCF elements is discussed in Section 3, and it is shown how ANCF elements can be used with cubic spline function representation to define the geometry of the rigid rails. In Section 4, the formulation of the liquid/tank interaction forces and the search method used in this investigation to define the fluid/tank contact points are described. In Section 5, the constitutive fluid model used in the total Lagrangian and non-incremental solution procedure adopted in this paper is briefly discussed. The integration of the liquid sloshing model in computational MBS railroad vehicle algorithms, the track geometry, and the three-dimensional wheel/rail contact force model are elaborated in Section 6. The components of the MBS vehicle model and the fluid model data used to examine the effect of liquid sloshing on the performance of the newly introduced ECP brake system and the rail vehicle dynamics during curve negotiations are also detailed in Section 6. In this investigation, the results obtained using the ECP braking force model are compared with the results obtained using the conventional air brake system. In order to improve the efficiency of the simulation, integration techniques such as the Hilber-Hughes-Taylor (HHT) method [3] and reduced integration when calculating the fluid viscous forces are used. The numerical results are presented in Section 7, while summary and conclusions drawn from this study are presented in Section 8.

2. BASIC INERTIA FORCE DEFINITIONS

A rail vehicle can safely negotiate a curve if the outward inertia force does not exceed the sum of the lateral gravity force component and the inward friction force. However, the centrifugal force of a flexible body does not take the simple form of mV^2/R, where m is the mass of the vehicle, V is the forward velocity, and R is the radius of curvature of the curve [28]. A straightforward method to determine the outward inertia force in the case of flexible body dynamics is to use the projection of the inertia force vector on the outward normal to the curve, which has the form $\int_{V^i} \rho^i \ddot{\mathbf{r}}^i dV^i \cdot \mathbf{n}$ in the case of a flexible body i, where ρ^i and V^i are, respectively, the mass density and volume of the flexible body, $\ddot{\mathbf{r}}^i$ is the acceleration vector, and $\mathbf{n}$ is the outward unit normal to the curve. This inertia force expression is general and includes the effect of other deformation-dependent forces such as gyroscopic moments and Coriolis forces.

2.1 FFR Inertia Forces

The form of the inertia forces depends on the method used to formulate the kinematic and dynamic equations. When ANCF elements are used, the inertia forces take a simple form and the mass matrix becomes constant. While ANCF elements will be used in this investigation, another widely used formulation, the floating frame of reference (FFR), is used in this section to shed light on the form of the inertia forces in the case of curve negotiation and to show that the rigid body assumption leads to the definition of the centrifugal forces used in rigid body dynamics. To this end, a simple planar example is used in this section [28].

Unlike the ANCF description, in the FFR formulation, a flexible body coordinate system is introduced and the motion of a planar body i in the system is defined using two coupled sets of coordinates, the reference coordinates $\mathbf{q}_r^i = \begin{bmatrix} \mathbf{R}^{i\mathrm{T}} & \theta^i \end{bmatrix}^{\mathrm{T}}$ and the elastic coordinates $\mathbf{q}_f^i$, where $\mathbf{R}^i$ describes the body reference translation, θ^i defines the reference orientation, and $\mathbf{q}_f^i$ defines the body deformation with respect to its reference. In the FFR formulation, there is no separation between the rigid body motion and the elastic deformation, and therefore, the FFR description does not imply any simplifying assumptions. The generalized coordinates for a planar deformable body i can then be written as $\mathbf{q}^i = \begin{bmatrix} \mathbf{R}^{i\mathrm{T}} & \theta^i & \mathbf{q}_f^{i\mathrm{T}} \end{bmatrix}^{\mathrm{T}}$. Using these generalized coordinates, the global position vector of an arbitrary point on the deformable body can be written as

$$\mathbf{r}^i = \mathbf{R}^i + \mathbf{A}^i \bar{\mathbf{u}}^i = \mathbf{R}^i + \mathbf{A}^i \left(\bar{\mathbf{u}}_o^i + \mathbf{S}^i \mathbf{q}_f^i \right) \qquad (1)$$

where $\bar{\mathbf{u}}^i$ is the local position vector defined in the body coordinate system, and $\mathbf{A}^i$ is the transformation matrix that defines the body orientation and is expressed in terms of the angle θ^i. The local position vector $\bar{\mathbf{u}}^i$ can be written as $\bar{\mathbf{u}}_o^i + \bar{\mathbf{u}}_f^i$, in which $\bar{\mathbf{u}}_o^i$ is local position vector of the arbitrary point in the undeformed state and $\bar{\mathbf{u}}^i_f$ is the deformation vector which can be written using the technique of the separation of variables as $\mathbf{S}^i\mathbf{q}^i_f$ in which $\mathbf{S}^i$ is a space-dependent shape function matrix. The acceleration vector can be derived by differentiating the position vector twice with respect to time as

$$\ddot{\mathbf{r}}^i = \ddot{\mathbf{R}}^i + \mathbf{A}^i_\theta \bar{\mathbf{u}}^i \ddot{\theta}^i + \mathbf{A}^i\mathbf{S}^i\ddot{\mathbf{q}}^i_f - \left(\dot{\theta}^i\right)^2 \mathbf{A}^i\bar{\mathbf{u}}^i + 2\dot{\theta}^i\mathbf{A}^i_\theta\mathbf{S}^i\dot{\mathbf{q}}^i_f \tag{2}$$

Substituting this equation into the inertia force expression, one obtains

$$\int_{V^i}\rho^i\ddot{\mathbf{r}}^i dV^i = m^i\ddot{\mathbf{R}}^i + \mathbf{A}^i_\theta\left(\mathbf{I}^i_1 + \bar{\mathbf{S}}^i\mathbf{q}^i_f\right)\ddot{\theta}^i + \mathbf{A}^i\bar{\mathbf{S}}^i\ddot{\mathbf{q}}^i_f - \left(\dot{\theta}^i\right)^2\mathbf{A}^i\left(\mathbf{I}^i_1 + \bar{\mathbf{S}}^i\mathbf{q}^i_f\right) + 2\dot{\theta}^i\mathbf{A}^i_\theta\bar{\mathbf{S}}^i\dot{\mathbf{q}}^i_f \tag{3}$$

where $\mathbf{I}^i_1 = \int_{V^i}\rho^i\bar{\mathbf{u}}^i_o dV^i$, $\bar{\mathbf{S}}^i = \int_{V^i}\rho^i\mathbf{S}^i dV^i$, and in the case of planar motion, the transformation matrix and its partial derivative are given, respectively, as

$$\mathbf{A}^i = \begin{bmatrix}\cos\theta^i & -\sin\theta^i \\ \sin\theta^i & \cos\theta^i\end{bmatrix}, \qquad \mathbf{A}^i_\theta = \begin{bmatrix}-\sin\theta^i & -\cos\theta^i \\ \cos\theta^i & -\sin\theta^i\end{bmatrix} \tag{4}$$

If the flexible body negotiates a circular curve with a constant forward velocity, as shown in Fig. 1, the motion constraints are defined as $\mathbf{R}^i - R\begin{bmatrix}\sin\theta^i & -\cos\theta^i\end{bmatrix}^{\mathrm{T}} = \mathbf{0}$, where R is the radius of curvature. In this special planar case, the unit outward normal to the curve takes the form $\mathbf{n} = \begin{bmatrix}\sin\theta^i & -\cos\theta^i\end{bmatrix}^{\mathrm{T}}$. If the arc length traveled by the reference point is defined as s^i, then the constraints at the acceleration level are written as

$$\ddot{\mathbf{R}}^i = \ddot{s}^i\begin{bmatrix}\cos\theta^i \\ \sin\theta^i\end{bmatrix} + \frac{\left(\dot{s}^i\right)^2}{R}\begin{bmatrix}-\sin\theta^i \\ \cos\theta^i\end{bmatrix} \tag{5}$$

in which the identities $\dot{\theta}^i = \dot{s}^i/R$ and $\ddot{\theta}^i = \ddot{s}^i/R$ are used. Using the preceding equations with the outward inertia force $F^i = \int_{V^i}\rho^i\ddot{\mathbf{r}}^i dV^i\cdot\mathbf{n}$, and assuming a constant forward velocity (that is, $\ddot{s}^i = 0$), one obtains

$$F^i = -m^i \frac{\left(\dot{s}^i\right)^2}{R} + \begin{bmatrix} 0 \\ -1 \end{bmatrix}^{\mathrm{T}} \bar{\mathbf{S}}^i \ddot{\mathbf{q}}_f^i - \left(\frac{\dot{s}^i}{R}\right)^2 \begin{bmatrix} 0 \\ -1 \end{bmatrix}^{\mathrm{T}} \left(\mathbf{I}_1^i + \bar{\mathbf{S}}^i \mathbf{q}_f^i\right) + 2\frac{\dot{s}^i}{R} \begin{bmatrix} -1 \\ 0 \end{bmatrix}^{\mathrm{T}} \bar{\mathbf{S}}^i \dot{\mathbf{q}}_f^i \tag{6}$$

In the case of steady state motion, where $\ddot{\mathbf{q}}_f^i = \mathbf{0}$ and $\dot{\mathbf{q}}_f^i = \mathbf{0}$, the preceding equation reduces to $F^i = -m^i \left(\dot{s}^i\right)^2 / R + \left(\dot{\theta}^i\right)^2 \left[0 \quad 1\right]^{\mathrm{T}} \left(\mathbf{I}_1^i + \bar{\mathbf{S}}^i \mathbf{q}_f^i\right)$, which shows that, even when the time derivatives of the elastic coordinates are zeros, the outward inertia force of a deformable body depends on the deformation and differs from $m^i \left(\dot{s}^i\right)^2 / R$ used in rigid body dynamics. In the case of a rigid body with a centroidal body coordinate system, $\mathbf{I}_1^i$ and $\mathbf{q}_f^i$ vanish, and F^i reduces to $F^i = -m^i \left(\dot{s}^i\right)^2 / R$, which demonstrates clearly that the centrifugal force in the case of rigid body dynamics is a special case of the more general expression used in flexible body dynamics. The FFR analysis presented in this section sheds light on the fundamental differences between the inertia force definitions used in rigid and flexible body dynamics. These fundamental differences must be considered in the case of liquid sloshing in railroad vehicles which experience large displacements.

2.2 ANCF Inertia Forces

In this investigation, three-dimensional ANCF elements are used in the analysis of liquid sloshing, and therefore, the general expression of the outward inertia force $\int_{V^i} \rho^i \ddot{\mathbf{r}}^{i\mathrm{T}} \mathbf{n} dV^i$ will be used. The displacement field of an ANCF element j is defined in the global coordinate system as $\mathbf{r}^{ij} = \mathbf{S}^{ij}\mathbf{e}^{ij}$, where $\mathbf{S}^{ij}$ is the element shape function matrix and $\mathbf{e}^{ij}$ is the vector of the ANCF element nodal coordinates. Because in the ANCF kinematic description, a body (structure) coordinate system is not used, direct comparison with rigid body dynamics cannot be easily made as in the case of the FFR formulation. Nonetheless, one can show the equivalence of the ANCF and FFR kinematic description. One can also show that $\int_{V^i} \rho^i \ddot{\mathbf{r}}^{i\mathrm{T}} \mathbf{n} dV^i = m^i \ddot{\mathbf{r}}_c^{i\mathrm{T}} \mathbf{n}$, in which m^i is the total mass of the ANCF flexible body and $\ddot{\mathbf{r}}_c^i$ is the acceleration vector of the body center of mass. The constant mass matrix of element j of the ANCF flexible body i is defined as $\mathbf{m}^{ij} = \int_{V^{ij}} \rho^{ij} \mathbf{S}^{ij^{\mathrm{T}}} \mathbf{S}^{ij} dV^{ij}$, where $\mathbf{S}^{ij}$ is space-dependent shape function matrix, ρ^{ij} is the element density, and V^{ij} is the element volume [26]. The position vector of the center of mass can be written as $\mathbf{r}_c^i = \left(\sum_{j=1}^{n_e} \bar{\mathbf{S}}^{ij} \mathbf{e}^{ij} \right) \Big/ m^i$, where $m^i = \sum_{j=1}^{n_e} m^{ij}$, m^{ij} is the mass of element j, $\bar{\mathbf{S}}^{ij} = \int_{V^{ij}} \rho^{ij} \mathbf{S}^{ij} dV^{ij}$, and n_e is the total number of elements. It follows that $\ddot{\mathbf{r}}_c^i = \left(\sum_{j=1}^{n_e} \bar{\mathbf{S}}^{ij} \ddot{\mathbf{e}}^{ij} \right) \Big/ m^i$. In order to define the outward inertia force for the liquid body, the unit outward normal $\mathbf{n}^i$ to the curve should also be defined.

3. INTEGRATION OF GEOMETRY AND ANALYSIS FOR RAILROAD SLOSHING

In railroad vehicle system applications, accurate definition of the liquid/tank geometry and wheel/rail geometry, shown in Fig. 2, is necessary for thorough investigation of the sloshing effect. In this investigation, ANCF elements are used to describe both the track and liquid/tank geometry. The track geometry is described using ANCF beam elements, while the liquid and tank are modeled using ANCF solid elements. The wheel is modeled as a surface of revolution, and therefore, no FE discretization is required. The procedure described in this section allows for the use of a unified geometry/analysis mesh from the outset for the study of the liquid sloshing as well as the wheel/rail contact.

3.1 ANCF Track Geometry

The wheel/rail contact forces that define the vehicle stability depend on the geometry of the wheel and rail profiles. The wheels and rails can be modeled as rigid or flexible bodies depending on the focus of the investigations. The track can be tangent (straight line) or curved; curved tracks are formed using constant radius and spiral segments. The spiral sections are designed to have a curvature that varies linearly along the spiral arc length, thereby allowing smoothly joining a tangent track segment with a circular segment. Figure 3 shows a three-dimensional fully parameterized ANCF beam element used in this investigation to describe the geometry of a curved track segment. The geometry of the rail segment is defined by the geometry of the space curve and the profile geometry. The three-dimensional fully parameterized ANCF beam element used in this study has at each node 12 coordinates that contain positions and position vector gradients; that is, for a node k, the vector of coordinates is defined as $\mathbf{e}^{ijk} = \begin{bmatrix} \mathbf{r}^{ijk^{\mathrm{T}}} & \mathbf{r}_x^{ijk^{\mathrm{T}}} & \mathbf{r}_y^{ijk^{\mathrm{T}}} & \mathbf{r}_z^{ijk^{\mathrm{T}}} \end{bmatrix}^{\mathrm{T}}, k = 1,2$, where $\mathbf{r}_\alpha^{ijk} = \partial \mathbf{r}^{ijk} / \partial \alpha, \alpha = x, y, z$, $\mathbf{r}^{ijk}$ is the global position vector at node k, and x, y, and z are the element spatial coordinates [26]. In the case of a fully parameterized beam element, the parameters x, y, and z are independent and can be used to define the three independent position gradient vectors $\mathbf{r}_\alpha^{ijk} = \partial \mathbf{r}^{ijk} / \partial \alpha, \alpha = x, y, z$. In railroad vehicle dynamics, the profile of the rail is measured using a device called a mini-prof that produces cubic spline data which define the profile geometry. Therefore, the surface of the rail can be described using the parametric expression $y = f(z)$. If the profile geometry changes along the rail space curve, the more general parametric equation $y = f(x, z)$ can be used. The profile geometry defined by the parametric equation $y = f(x, z)$ can be integrated systematically with the fully parameterized ANCF beam element to define the rail surface geometry at the contact points. The rail surface geometry is used in the numerical solution algorithm to define the location of the wheel/rail contact points, the velocity creepages, and the creep contact forces. The definition of these kinematic and force variables requires the definition of the tangent plane and the normal vector to this plane. If s^r defines the rail arc length and y defines the lateral rail parameter, one can define the longitudinal and lateral tangent vectors at an arbitrary point on the rail surface using the ANCF kinematic equations $\mathbf{r}_{s^r}^{ij} = \left(\partial \mathbf{r}^{ij} / \partial x\right)\left(\partial x / \partial s^r\right)$, and $\mathbf{r}_y^{ij} = \left(\partial \mathbf{r}^{ij} / \partial y\right) + \left(\partial \mathbf{r}^{ij} / \partial x\right)\left(\partial x / \partial y\right) + \left(\partial \mathbf{r}^{ij} / \partial z\right)\left(\partial z / \partial y\right)$, respectively. The unit normal vector to the rail surface that corresponds to element j can be defined as $\mathbf{n}^{ij} = \left(\partial \mathbf{r}_{s^r}^{ij} \times \partial \mathbf{r}_y^{ij}\right) / \left|\partial \mathbf{r}_{s^r}^{ij} \times \partial \mathbf{r}_y^{ij}\right|$. If the rail is assumed rigid, the nodal coordinates of the element are constants and assume their initial values. If the rail is assumed flexible, the nodal coordinates will change with time in response to the wheel/rail contact forces. Therefore, the ANCF geometry description presented in this section can be applied to both rigid and flexible rails. However, because the focus of this investigation is on railroad liquid sloshing, the rail is assumed to be rigid.

3.2 Liquid/Tank Geometry

In this section, an initially curved ANCF fluid, shaped according to the rail tank-car geometry, is modeled using fully parameterized ANCF solid elements. The tank is assumed to consist of a cylinder with half-ellipsoid ends, as shown in Fig. 4. The tank-car and the fluid geometries enter into the definition of the fluid/tank contact forces formulated in this investigation using a penalty method in which both the normal and friction forces are considered. Because the liquid has relatively larger deformation than the tank, the tank is assumed to be rigid in this study.

In order to define an initially curved fluid geometry/analysis mesh consistent with the geometry of the railroad tank which consists of a cylinder and two half-ellipsoid ends, it is required that the fluid mesh at the boundary has the same curved shape as the tank. Wei et al. [33] demonstrated that fewer ANCF fluid elements can describe the fluid motion compared with the FFR formulation. The solid element used in this investigation is a fully parameterized ANCF element with 8 nodes; each node has 12 coordinates, $\mathbf{e}^{ijk} = \begin{bmatrix} \mathbf{r}^{ijk^{\mathrm{T}}} & \mathbf{r}_x^{ijk^{\mathrm{T}}} & \mathbf{r}_y^{ijk^{\mathrm{T}}} & \mathbf{r}_z^{ijk^{\mathrm{T}}} \end{bmatrix}^{\mathrm{T}}, k = 1, 2, \ldots, 8$ [16, 26]. The initially curved ANCF solid elements are used to model the fluid inside the tank with a cross-section geometry defined by eight elements, as shown in Fig. 5, where in this figure, r is the radius of the cylindrical tank, h is a measure of the height of the liquid free surface, and the angular parameters θ, α, β and γ are used to determine nodal positions and gradients. In Fig. 5, the nodes and element numbers are labeled such that the nodes with solid circles represent the element master nodes used to define the element dimensions; examples of master nodes are shown where node 1 in Fig. 6a is the master node for the straight element and node 2 in Fig. 6b is the master node for an initially curved element. The element dimensions in the reference configuration are assumed a, b, and c as shown in Fig. 6b. The ANCF gradient vectors can be conveniently used for efficient shape manipulation in order to accurately define the fluid geometry; for example, if there is no stretch or change of shape at a node of the fluid, the gradients will assume values that correspond to the straight configuration, that is, $\begin{bmatrix} 1 & 0 & 0 \end{bmatrix}^{\mathrm{T}}$ for the first gradient vector $\mathbf{r}_x^{ijk}$, $\begin{bmatrix} 0 & 1 & 0 \end{bmatrix}^{\mathrm{T}}$ for the second gradient vector $\mathbf{r}_y^{ijk}$, and $\begin{bmatrix}0 & 0 & 1\end{bmatrix}^{\mathrm{T}}$ for the third gradient vector $\mathbf{r}_z^{ijk}$. In the case of an element that has a reference configuration different from the straight configuration, as in Fig. 6b, the gradients can be adjusted to properly define the desired geometry. For example, referring to the geometry of the fluid mesh in Figs. 5 and 6, the gradients in the reference configuration can be obtained as $\mathbf{r}_z^4 = \begin{bmatrix}0 & 1 & 0\end{bmatrix} \cdot \left(l_{67}/c\right)$, $\mathbf{r}_y^5 = \begin{bmatrix}0 & -\sin\theta & -\cos\theta\end{bmatrix}^{\mathrm{T}} \cdot \left(l_{16}/b\right)$, and $\mathbf{r}_y^8 = \begin{bmatrix}0 & -\cos\alpha & -\sin\alpha\end{bmatrix}^{\mathrm{T}} \cdot \left(l_{16}/b\right)$, where the superscript ij is dropped for simplicity, the number superscript refers to the node number, and the angles θ and α and the arc lengths l_{67} and l_{16} can be determined according to the free surface height h and radius of the cylinder r. Figure 7 shows the complete mesh of the fluid inside a tank; the mesh has 75 nodes, 32 elements, and a total of 900 degrees of freedom.

4. FLUID/TANK INTERACTION FORCES

The penalty method is used in this investigation to formulate the fluid/tank interaction forces that produce the sloshing oscillations. The boundary surfaces of the fluid mesh are regarded as the potential contact surfaces and points on these surfaces are monitored throughout the simulation in order to determine the contact points. It will be explained later in this section how the contact points are identified in the case of the cylindrical tank and also in the case of the tank ellipsoidal ends whose geometry is important, particularly in the case of sudden braking application.

4.1 Normal Contact Force

The penalty forces, which include normal and tangential friction forces, are applied on both the fluid and the tank bodies only when interpenetration occurs. A contact frame at the contact point is introduced in order to define the normal and tangential forces along the axes of this contact frame. Knowing the relative penetration δ, and its time rate $\dot{\delta}$, between the fluid ANCF element and the tank at the contact point, the normal contact force can be evaluated using the formula $f_n = -K\delta^{1.5} - C\dot{\delta}|\delta|$, where K and C are the penalty coefficients associated with the penetration and the penetration rate, respectively, and $|\cdot|$ represents the absolute value. In the expression used in this investigation for the normal force, the exponent on the penetration in the stiffness term was chosen to be 1.5 to increase smoothness near zero penetration. Other force models, including a linear relationship, can also be used. The absolute value term is included in the damping term to ensure that the normal force is equal to 0 when there is no penetration. It follows that the tangential friction force can be written as $f_t = \mu f_n$, where μ is the coefficient of friction between the fluid and tank at the interface. Determining the friction coefficient between a fluid and solid surface is not a trivial matter, and is not the focus of this work. It is a function of the texture of the solid surface as well as the viscosity of the fluid, and is highly sensitive to changes in the liquid-solid interface [17, 19]. A relatively large value of $\mu = 0.5$ was chosen to reduce relative motion between the fluid and solid surfaces and approximate the no-slip condition characteristic of viscous Newtonian fluids [34].

4.2 Relative Position

The position vector of a potential contact point P on ANCF solid element j of the fluid body f can be written as $\mathbf{r}_P^{fj} = \mathbf{S}_P^{fj}\mathbf{e}^{fj}$, where $\mathbf{S}_P^{fj}$ is the shape function matrix evaluated at point P, and $\mathbf{e}^{fj}$ is the vector of nodal coordinates of the ANCF element j. If the global position vector of the origin of the coordinate system of the rigid tank body t is defined as $\mathbf{R}^t$, the relative position and velocity vectors of the potential contact point on the fluid with respect to the tank can be written as $\mathbf{u}_P^{ft} = \mathbf{r}_P^f - \mathbf{R}^t$ and $\dot{\mathbf{u}}_P^{ft} = \dot{\mathbf{r}}_P^f - \dot{\mathbf{R}}^t$, respectively. In order to define the penetration δ and the penetration rate $\dot{\delta}$, the relative position vector $\mathbf{u}_P^{ft} = \mathbf{r}_P^f - \mathbf{R}^t$ is defined in the local tank body coordinate system as $\bar{\mathbf{u}}_P^{ft} = \mathbf{A}^{t^{\mathrm{T}}} \mathbf{u}_P^{ft} = \mathbf{A}^{t^{\mathrm{T}}} \left(\mathbf{r}_P^f - \mathbf{R}^t \right)$, where $\mathbf{A}^t$ is the transformation matrix that defines the orientation of the tank coordinate system in the global coordinate system. Similarly, the relative velocity between the contact points on the fluid and tank bodies can be written as $\mathbf{v}_{Pr}^{ft} = \mathbf{A}^{t^{\mathrm{T}}} \left(\dot{\mathbf{u}}_P^{ft} - \tilde{\boldsymbol{\omega}}^t \mathbf{u}_P^{ft} \right)$, where $\tilde{\boldsymbol{\omega}}^t$ is the skew-symmetric matrix that defines the tank absolute angular velocity vector $\boldsymbol{\omega}^t$. The relative position and velocity vectors at the potential contact point can be used to define the penetration δ and its rate $\dot{\delta}$. The origin of the body coordinate system of the tank is chosen to be at the tank geometric center, as shown in Fig. 8. Using the symmetry of the tank, the tank can be divided into two geometry sections, the cylindrical and ellipsoidal sections. The cylindrical section has length L and radius r, while the three axes of the half-ellipsoid are defined as a, b, and c, and satisfy the relationship $b = c = r$. Two local coordinate systems, $x_c^t y_c^t z_c^t$ and $x_e^t y_e^t z_e^t$, are introduced for the cylindrical and ellipsoidal sections, respectively, for the convenience of defining the normal and tangential contact forces at the contact point.

4.3 Cylindrical Region

In the case that the contact occurs in the cylindrical section of the tank, the normal vector at the contact point $\mathbf{n}_P^t$ is simply directed to the tank center and can be defined as $\mathbf{n}_P^t = \begin{bmatrix} 0 & -\bar{u}_{P2}^{ft} & -\bar{u}_{P3}^{ft} \end{bmatrix}^{\mathrm{T}}$, where $\bar{u}_{Pl}^{ft}, l = 1,2,3$, are the three components of the vector $\bar{\mathbf{u}}_P^{ft}$ defined in the tank cylindrical section coordinate system $x_c^t y_c^t z_c^t$ as shown in Fig. 8. The unit normal vector at the contact point $\hat{\mathbf{n}}_P^t = \mathbf{n}_P^t \big/ \sqrt{\mathbf{n}_P^{t\,\mathrm{T}} \mathbf{n}_P^t}$ can be used to define the tangential relative velocity vector as $\left(\mathbf{v}_{Pr}^{ft}\right)_t = \mathbf{v}_{Pr}^{ft} - \left(\mathbf{v}_{Pr}^{ft} \cdot \hat{\mathbf{n}}_P^t\right)\hat{\mathbf{n}}_P^t$. A unit vector along the tangential relative velocity can be defined as $\mathbf{t}_P^t = \left(\mathbf{v}_{Pr}^{ft}\right)_t \big/ \left|\left(\mathbf{v}_{Pr}^{ft}\right)_t\right|$. Using these definitions, the penetration and penetration rate can be defined, respectively, as $\delta = \sqrt{\mathbf{n}_P^{t\,\mathrm{T}} \mathbf{n}_P^t} - r$ and $\dot{\delta} = \mathbf{v}_{Pr}^{ft} \cdot \hat{\mathbf{n}}_P^t$. If $\delta > 0$, the normal contact and friction forces at the contact point can be evaluated, respectively, as $f_n = -K\delta^{3/2} - C\dot{\delta}\left|\delta\right|$ and $f_t = \mu f_n$, respectively. Therefore, the penalty force vector can be written as $\mathbf{f}_P = f_n \hat{\mathbf{n}}_P^t - f_t \mathbf{t}_P^t$. This penalty force vector can be defined in the global coordinate system as $\mathbf{F}_P = \mathbf{A}^t \mathbf{f}_P$. The generalized contact forces exerted on element j of the ANCF fluid body can be defined using the virtual work and can be written as $\mathbf{Q}_P^{fj} = \mathbf{S}_P^{fj\,\mathrm{T}} \mathbf{F}_P = \mathbf{S}_P^{fj\,\mathrm{T}} \mathbf{A}^t \mathbf{f}_P$. In this equation, $\mathbf{Q}_P^{fj}$ is the vector of generalized forces associated with the ANCF nodal coordinates of the fluid element j. The resultant contact forces on the rigid tank are equal in magnitude but opposite in direction to the forces exerted on the fluid. The generalized contact forces associated with the generalized coordinates of the rigid tank is $\mathbf{Q}_P^{t\,\mathrm{T}} = -\begin{bmatrix} \mathbf{F}_P^{\mathrm{T}} & -\mathbf{F}_P^{\mathrm{T}} \mathbf{A}^t \tilde{\bar{\mathbf{u}}}_P^t \bar{\mathbf{G}}^{t\mathrm{T}} \end{bmatrix}$, where $\bar{\mathbf{G}}^t$ is the transformation matrix which relates the angular velocity vector to the time derivatives of the orientation parameters, $\bar{\boldsymbol{\omega}}^t = \bar{\mathbf{G}}^t \dot{\boldsymbol{\theta}}^t$, $\tilde{\bar{\mathbf{u}}}_P^t$ is the skew matrix associated with the vector $\bar{\mathbf{u}}_P^t$ which defines the contact point on the tank in the tank coordinate system and can be written as $\bar{\mathbf{u}}_P^t = r\hat{\mathbf{n}}_P^t + \begin{bmatrix} \bar{u}_{P1}^{ft} & 0 & 0 \end{bmatrix}^{\mathrm{T}}$, $\bar{\boldsymbol{\omega}}^t$ is the absolute angular velocity vector of the tank reference defined in the tank coordinate system, and $\boldsymbol{\theta}^t$ is the set of parameters used to define the orientation of the tank coordinate system. In this investigation, Euler parameters are used as the orientation coordinates.

4.4 Ellipsoidal Region

In the case that the contact occurs in the ellipsoidal sections of the tank, which can be determined by evaluating $\left|\bar{u}_{P1}^{ft}\right| > L/2$, the relative position and velocity vectors of the contact point can be defined with respect to the coordinate system $x_e^t y_e^t z_e^t$ which is located at the ellipsoid center as shown in Fig. 8. By introducing the analytical expression of an ellipsoid, one can check if the condition $\left(\bar{u}_{P1}^{ft}/a\right)^2 + \left(\bar{u}_{P2}^{ft}/b\right)^2 + \left(\bar{u}_{P3}^{ft}/c\right)^2 > 1$ is satisfied to determine if a contact occurs between the fluid and the half-ellipsoids. Assuming that the position vector of the contact point on the tank wall $\bar{\mathbf{u}}_P^t$ with respect to the origin of the tank coordinate system is parallel to the vector $\bar{\mathbf{u}}_P^{ft}$ which defines the location of the contact point on the fluid in the same coordinate system, one can calculate $\bar{\mathbf{u}}_P^t$ by using the ellipsoid geometry function. The normal vector at the potential contact point can be written as $\mathbf{n}_P^t = -2\left[\bar{u}_{P1}^{ft}/a^2 \quad \bar{u}_{P2}^{ft}/b^2 \quad \bar{u}_{P3}^{ft}/c^2\right]^{\mathrm{T}}$. Having determined the normal vector, a procedure similar to the one used for the tank cylindrical section can be used to determine the normal and tangential velocity components as well as the penetration δ and its rate $\dot{\delta}$. Using this information, the normal and tangential friction forces can be calculated and used to determine the generalized forces associated with the generalized coordinates of the ANCF fluid and rigid tank bodies.

5. ANCF FLUID CONSTITUTIVE EQUATIONS

In order to demonstrate the use of the general procedure proposed in this investigation, an incompressible Newtonian fluid model is used, where the viscous forces as well as the incompressibility conditions of the fluid can be formulated systematically based on the Navier-Stokes equations. The resultant stresses are used to define the generalized viscous forces of the ANCF fluid element. Using higher-order ANCF solid elements, fewer elements are needed to model the liquid sloshing compared to the conventional FE method and the FE/FFR approach [31]. These ANCF elements can also accurately capture the initial shape as well as the complex shapes that result from the liquid sloshing as previously explained in this paper.

In order to consider the initially curved configuration of a fluid element that interacts with a curved tank surface, the relationships between the volumes in various configurations should first be defined. Let V, V_o, and v be the volumes in the straight, curved reference, and current deformed configurations, respectively, and $\mathbf{x}$, $\mathbf{X}$, and $\mathbf{r}$ are the corresponding position vectors of an arbitrary fluid point in these three configurations. The position vectors in the reference and current configurations are written, respectively, as $\mathbf{X} = \mathbf{S}\mathbf{e}_o$ and $\mathbf{r} = \mathbf{S}\mathbf{e}$, in which $\mathbf{S}$ is the shape function matrix and $\mathbf{e}_o$ and $\mathbf{e}$ are the nodal position vectors defined in the reference and current configurations, respectively. The relation between the volume in the initially curved reference configuration and the volume in the straight configuration can be defined as $dV_o = |\mathbf{J}_o| dV$, where $|\cdot|$ refers to the determinant of a matrix and $\mathbf{J}_o$ is the constant Jacobian matrix of the position vector gradients and is defined as

$\mathbf{J}_o = \partial \mathbf{X} / \partial \mathbf{x} = \partial(\mathbf{S}\mathbf{e}_o)/\partial \mathbf{x} = \mathbf{S}_\mathbf{x} : \mathbf{e}_o$, in which $\mathbf{S}_\mathbf{x} = \partial \mathbf{S}/\partial \mathbf{x}$ is a third-order tensor that defines the derivatives of the shape function matrix with respect to the straight configuration parameters $\mathbf{x}$. The relationship between the volume defined in the current configuration and the volume in the curved reference configuration can be written as $dv = |\mathbf{J}| dV_o$, where $\mathbf{J}$ is the Jacobian matrix of position vector gradients defined as $\mathbf{J} = \partial \mathbf{r}/\partial \mathbf{X} = (\partial \mathbf{r}/\partial \mathbf{x})(\partial \mathbf{x}/\partial \mathbf{X}) = \mathbf{J}_e \mathbf{J}_o^{-1}$, in which $\mathbf{J}_e = \partial \mathbf{r}/\partial \mathbf{x} = \partial(\mathbf{S}\mathbf{e})/\partial \mathbf{x} = \mathbf{S}_\mathbf{x} : \mathbf{e}$. It follows that $dv = |\mathbf{J}||\mathbf{J}_o| dV = |\mathbf{J}_e \mathbf{J}_o^{-1}||\mathbf{J}_o| dV = |\mathbf{J}_e| dV$. Therefore, integrations carried out over the initially curved reference configuration domain can be systematically converted to integrations over the straight configuration domain, allowing for using the element dimensions defined in the initially straight configuration throughout the entire simulation regardless of the amount of the fluid displacements. Using the principle of conservation of mass, the density defined in the initial straight configuration can be used.

5.1 Viscosity and Penalty Forces

The penalty method is used in this investigation to impose the incompressibility condition of the fluid elements. For an incompressible fluid element j, the determinant of the matrix of position vector gradients must be equal to one, that is $J^j = |\mathbf{J}^j| = 1$ and its first derivative $\dot{J}^j = 0$. In this case, the Navier-Stokes stress relationship reduces to $\boldsymbol{\sigma}^j = 2\mu_f \mathbf{D}^j$, where $\mathbf{D}^j$ is the rate of deformation tensor, $\boldsymbol{\sigma}^j$ is the symmetric Cauchy stress tensor, and μ_f is the coefficient of shear viscosity [29, 26]. In this investigation, the mass density remains constant because of the incompressibility condition, and the effect of temperature is neglected. In general, the virtual work of the fluid viscous forces can be written in terms of the second Piola-Kirchoff stress tensor

$\boldsymbol{\sigma}_{P2}^j$ and Green-Lagrangian Strain tensor $\boldsymbol{\varepsilon}^j$ since they are defined in the reference configuration as $\delta W_v^j = -\int_{v^j} \boldsymbol{\sigma}^j : \delta \mathbf{J}^j \mathbf{J}^{j^{-1}} dv^j = -\int_{V_o^j} \boldsymbol{\sigma}_{P2}^j : \delta \boldsymbol{\varepsilon}^j dV_o^j$ in which $\boldsymbol{\varepsilon}^j = \left(\mathbf{J}^{j^{\mathrm{T}}} \mathbf{J}^j - \mathbf{I}\right) / 2$ and $\boldsymbol{\sigma}_{P2}^j = J^j \mathbf{J}^{j^{-1}} \boldsymbol{\sigma}^j \left(\mathbf{J}^{j^{-1}}\right)^{\mathrm{T}}$. In order to define the fluid viscous forces, the constitutive model $\boldsymbol{\sigma}^j = 2\mu_f \mathbf{D}^j$ and the kinematic relationship $\mathbf{D}^j = \left(\mathbf{J}^{j^{-1}}\right)^{\mathrm{T}} \dot{\mathbf{J}}^j \mathbf{J}^{j^{-1}}$ are used leading to

$$
\begin{aligned}
\delta W_v^j &= -\int_{V_o^j} \left(2\mu_f J^j \mathbf{J}^{j^{-1}} \left(\mathbf{J}^{j^{-1}}\right)^{\mathrm{T}} \dot{\mathbf{J}}^j \mathbf{J}^{j^{-1}} \left(\mathbf{J}^{j^{-1}}\right)^{\mathrm{T}} \right) : \delta \boldsymbol{\varepsilon}^j dV_o^j \\
&= -\int_{V_o^j} 2\mu_f J^j \left(\mathbf{C}_r^{j^{-1}} \dot{\mathbf{C}}_r^j \mathbf{C}_r^{j^{-1}} \right) : \delta \boldsymbol{\varepsilon}^j dV_o^j
\end{aligned}
\tag{7}
$$

where $\mathbf{C}_r^j = \mathbf{J}^{j^{\mathrm{T}}} \mathbf{J}^j$ is the right Cauchy-Green deformation tensor. Using the virtual work of the preceding equation, the viscous forces can be defined as

$$
\mathbf{Q}_v^j = -\int_{V_o^j} 2\mu_f J^j \left(\mathbf{C}_r^{j^{-1}} \dot{\mathbf{C}}_r^j \mathbf{C}_r^{j^{-1}} \right) : \frac{\partial \boldsymbol{\varepsilon}^j}{\partial \mathbf{e}^j} dV_o^j \tag{8}
$$

Since this integral is defined in the curved reference configuration, the volume relationship defined in the preceding section can be used to change the domain of integration to the straight configuration.

In order to impose the incompressibility condition, the penalty method is applied at both the position and velocity levels, $J^j = 1$ and $\dot{J}^j = 0$, respectively. Assume that the strain energy and dissipation penalty functions can be written as $U_{IC}^j = (1/2) k_{IC} \left(J^j - 1\right)^2$ and $U_{TD}^j = (1/2) c_{TD} \left(\dot{J}^j\right)^2$, respectively, where k_{IC} and c_{TD} are the penalty coefficients. The associated penalty forces can be derived as $\mathbf{Q}_{IC}^j = \partial U_{IC}^j / \partial \mathbf{e}^j = k_{IC} \left(J^j - 1\right)\left(\partial J^j / \partial \mathbf{e}^j\right)$ and $\mathbf{Q}_{TD}^j = \partial U_{TD}^j / \partial \dot{\mathbf{e}}^j = c_{TD} \dot{J}^j \left(\partial \dot{J}^j / \partial \dot{\mathbf{e}}^j\right)$, where

$$
\partial J^j / \partial \mathbf{e}^j = \partial \dot{J}^j / \partial \dot{\mathbf{e}}^j = \mathbf{S}_x^{j^{\mathrm{T}}} \left(\mathbf{r}_y^j \times \mathbf{r}_z^j \right) + \mathbf{S}_y^{j^{\mathrm{T}}} \left(\mathbf{r}_z^j \times \mathbf{r}_x^j \right) + \mathbf{S}_z^{j^{\mathrm{T}}} \left(\mathbf{r}_x^j \times \mathbf{r}_y^j \right) \tag{9}
$$

and $\dot{J}^j = \operatorname{tr}\left(\mathbf{D}^j\right) J^j$, in which $\operatorname{tr}(\cdot)$ refers to the trace of a matrix, $\mathbf{S}_\alpha^j, \alpha = x, y, z$, refers to the partial derivative of the shape function matrix with respect to the coordinate α defined in the straight configuration, $\mathbf{r}_\alpha^j = \mathbf{S}_\alpha^j \mathbf{e}^j$ for $\alpha = x, y, z$, and $\mathbf{e}^j$ and $\dot{\mathbf{e}}^j$ are the element nodal coordinate and velocity vectors, respectively, defined in the current configuration. Consequently, the viscosity and penalty forces of the fluid element can be written as $\mathbf{Q}_s^j = \mathbf{Q}_v^j + \mathbf{Q}_{IC}^j + \mathbf{Q}_{TD}^j$.

5.2 Fluid Element Equations of Motion

The virtual work of the inertia forces of the fluid element j is written as $\delta W_i^j = \int_{v^j} \rho_v^j \ddot{\mathbf{r}}^j \cdot \delta \mathbf{r}^j dv^j = \mathbf{m}^j \ddot{\mathbf{e}}^j \cdot \delta \mathbf{e}^j$, where $\mathbf{m}^j = \int_{V^i} \rho_V^j \mathbf{S}^{j^{\mathrm{T}}} \mathbf{S}^j dV^j$, and ρ_v^j and ρ_V^j are the densities defined in the current and straight configuration, respectively, and they are related by the equation $\rho_V^j = \left|\mathbf{J}_e^j\right| \rho_v^j$. This demonstrates that the mass matrix is a constant and symmetric matrix regardless of the amount of the fluid displacement. The virtual work of the externally applied forces can also be written as $\delta W_e^j = \int_{v^j} \mathbf{f}_e^{j^{\mathrm{T}}} \cdot \delta \mathbf{r}^j dv^j = \mathbf{Q}_e^j \cdot \delta \mathbf{e}^j$, in which $\mathbf{Q}_e^j = \int_{V^j} \mathbf{S}^{j^{\mathrm{T}}} \mathbf{f}_e^j \left|\mathbf{J}_e^j\right| dV^j$ is defined as the body force applied on the fluid element; this force expression is obtained by using the relationship between the volumes in the current and straight configurations. Applying the principle of virtual work for the fluid element j, one obtains the element equations of motion as $\mathbf{m}^j \ddot{\mathbf{e}}^j = \mathbf{Q}_e^j - \mathbf{Q}_s^j$, where $\mathbf{Q}_e^j$ is the vector of the body forces and $\mathbf{Q}_s^j$ is the vector of the elastic forces.

6. INTEGRATION WITH MBS RAILROAD VEHICLE ALGORITHMS

The fluid model proposed in this paper is implemented in an MBS railroad vehicle algorithm in order to develop new liquid sloshing models with significant details. In this section, the detailed vehicle model used in this investigation is introduced, the track and wheel/rail profile geometries are discussed, and the three-dimensional elastic wheel/rail contact formulation which allows for wheel/rail separation is briefly explained.

6.1 MBS Vehicle Model

The railroad MBS vehicle model considered in this investigation is shown in Fig. 9 and consists of two trucks and one tank car, where each truck consists of two wheelsets, two equalizer bars, one stub sill, one frame, and one bolster. The MBS vehicle model is thus assumed to have 16 bodies including 15 rigid bodies and one flexible body representing the fluid. The equalizer bars are connected to the wheelsets by journal bearings, and the frames are connected to the equalizer bars using spring-damper elements that represent the primary suspension. The bolster is connected to the frame using a revolute joint, and the tank is assumed to be rigidly connected to the two stub sills which are connected to the lead and rear bolsters by spring-damper elements representing the secondary suspension. The dimensions and inertia properties of the trucks are the same as that presented in the literature [24]. The forward velocity of the vehicle is defined using a trajectory coordinate constraint function that allows the vehicle to negotiate both tangent and curved tracks. An elastic contact formulation that allows for wheel/rail separation is used to define the wheel/rail dynamic interaction in the MBS vehicle algorithm, that is, the wheel is assumed to have six degrees of freedom with respect to the rail [25]. The railroad vehicle model with a rigid tank-car has 67 degrees of freedom, while in the case of the fluid tank-car, the model has 900 additional degrees of freedom used to describe the liquid motion inside the tank.

6.2 Track Geometry and Wheel/Rail Profiles

In order to examine the effect of the liquid sloshing on the wheel/rail contact and vehicle response, different simulation scenarios are considered using different track geometries. A curved track is used to understand the effect of liquid sloshing on the vehicle dynamics when the vehicle negotiates a curve; Table 1 shows the data of the curved track used in this investigation. A tangent track is also used in the braking scenario to analyze the effect of liquid sloshing on the coupler forces. It is important to note that in the case of a flexible fluid model, the centrifugal forces do not take the simple form as in the case of the rigid tank-car, as previously mentioned in this paper. For this reason, it is important to perform simulations to determine if the liquid sloshing will affect the balance speed and the vehicle safety. The track is modeled as a rigid body with zero degrees of freedom for all of the simulation scenarios considered.

The wheel and rail profiles used in this investigation are the same as the profiles used by Sanborn et al. [23], the AAR-1B-WF which has a 1:20 taper in the tread section of the wheel and is commonly used with freight cars in North America, and UIC 60 rail profile. The diameter of the wheel is 914 mm, and both the wheel and rail profiles are assumed to be in unworn conditions. The tank used in this investigation has the same dimension used by Wang et al. [32] with a length of 11.9 m and radius of roughly 1.5 m for the cylindrical part, and has a maximum capacity of 15,000 gallons.

6.3 Wheel/Rail Contact

A three-dimensional elastic contact formulation is used to define the wheel/rail interaction forces.

This formulation allows for wheel/rail separation, and therefore, the wheel has six degrees of freedom with respect to the rail. The geometries of the wheel and rail contact surfaces are described using surface parameters, as shown in Fig. 2. The wheel surface parameters are referred to as $\mathbf{s}^w = \begin{bmatrix} s_1^w & s_2^w \end{bmatrix}^{\mathrm{T}}$, where s_1^w is the wheel profile surface parameter and s_2^w is the wheel radial surface parameter [25]. The rail surface parameters are referred to as $\mathbf{s}^r = \begin{bmatrix} s_1^r & s_2^r \end{bmatrix}^{\mathrm{T}}$, where s_1^r is the longitudinal surface parameter that describes the distance traveled and s_2^r is the rail profile surface parameter. The assumptions of non-conformal wheel/rail contact are used. In order to determine the contact point, the following four algebraic equations are formulated: $\mathbf{C}\left(\mathbf{s}^w, \mathbf{s}^r\right) = \begin{bmatrix} \mathbf{r}^{wr\mathrm{T}}\mathbf{t}_1^r & \mathbf{r}^{wr\mathrm{T}}\mathbf{t}_2^r & \mathbf{n}^{r\mathrm{T}}\mathbf{t}_1^w & \mathbf{n}^{r\mathrm{T}}\mathbf{t}_2^w \end{bmatrix}^{\mathrm{T}} = \mathbf{0}$. In this equation, $\mathbf{t}_l^k = \partial \mathbf{r}^k / \partial s_l^k$, $l = 1, 2;\ k = w, r$ are the tangent vectors to the surface at the contact point, $\mathbf{n}^r$ is the normal to the rail surface, and $\mathbf{r}^{wr} = \mathbf{r}^w - \mathbf{r}^r$ is the relative position between the potential contact points on the wheel and rail. The four nonlinear algebraic equations $\mathbf{C}\left(\mathbf{s}^w, \mathbf{s}^r\right) = \mathbf{0}$ can be solved for the four surface parameters. These four surface parameters are used to define the potential contact points on the wheel and rail. The wheel/rail penetration δ and the relative velocity $\dot{\delta}$ along the normal to the rail are defined, respectively, as $\delta = \mathbf{r}^{wr\mathrm{T}}\mathbf{n}^r$ and $\dot{\delta} = \dot{\mathbf{r}}^{wr\mathrm{T}}\mathbf{n}^r$. If there is a penetration between the wheel and rail, an elastic force model is used to define the normal force [25]. The normal force, the creepages, the dimensions of the contact ellipse, and the wheel and rail material properties are used to define the tangential creep force and spin moment using Kalker's USETAB subroutine [12]. The dimensions of the contact ellipse are determined using Hertz's contact theory which requires the evaluation of the principal curvatures. It is also important to point out that the nonlinear algebraic equations $\mathbf{C}\left(\mathbf{s}^{w},\mathbf{s}^{r}\right)=\mathbf{0}$ are used only to determine the geometric surface parameters and there are no constraint forces associated with these algebraic equation since wheel/rail separation is allowed. More details on the elastic contact formulation used in this study can be found in the literature [25].

6.4 MBS Equations of Motion

The general equations of motion for an MBS system that consists of rigid and flexible bodies, including bodies modeled using the ANCF formulation, can be written in terms of the rigid body reference coordinates $\mathbf{q}_r$, ANCF nodal coordinates $\mathbf{e}$, and the non-generalized surface parameters $\mathbf{s}$ used in the contact formulations, as [24, 27]

$$\begin{bmatrix} \mathbf{M}_r & \mathbf{0} & \mathbf{0} & \mathbf{C}_{\mathbf{q}_r}^{\mathrm{T}} \\ \mathbf{0} & \mathbf{M}_e & \mathbf{0} & \mathbf{C}_{\mathbf{e}}^{\mathrm{T}} \\ \mathbf{0} & \mathbf{0} & \mathbf{0} & \mathbf{C}_{\mathbf{s}}^{\mathrm{T}} \\ \mathbf{C}_{\mathbf{q}_r} & \mathbf{C}_{\mathbf{e}} & \mathbf{C}_{\mathbf{s}} & \mathbf{0} \end{bmatrix} \begin{bmatrix} \ddot{\mathbf{q}}_r \\ \ddot{\mathbf{e}} \\ \ddot{\mathbf{s}} \\ \boldsymbol{\lambda} \end{bmatrix} = \begin{bmatrix} \mathbf{Q}_r \\ \mathbf{Q}_e \\ \mathbf{0} \\ \mathbf{Q}_d \end{bmatrix} \tag{10}$$

where $\ddot{\mathbf{q}}_r$, $\ddot{\mathbf{e}}$, and $\ddot{\mathbf{s}}$ are, respectively, the second time derivatives of the reference, ANCF, and non-generalized coordinates; $\mathbf{M}_r$ and $\mathbf{M}_e$ are, respectively, the rigid body mass matrix and ANCF constant mass matrix; $\mathbf{C}_{\mathbf{q}_r}$, $\mathbf{C}_{\mathbf{e}}$, and $\mathbf{C}_{\mathbf{s}}$ are the Jacobian matrices of the constraint equations associated, respectively, with the reference, ANCF, and non-generalized coordinates; $\boldsymbol{\lambda}$ is the vector of Lagrange multipliers; $\mathbf{Q}_r$ and $\mathbf{Q}_e$ are, respectively, the vectors of generalized forces associated with the rigid and elastic coordinates, and $\mathbf{Q}_d$ is the quadratic velocity vector that results from the differentiation of the nonlinear algebraic constraint equations twice with respect to time. The numerical procedure used in this investigation ensures that the nonlinear algebraic constraint equations are satisfied at the position, velocity, and acceleration levels. A flowchart depicting the numerical solution procedure is shown in Fig. 10.

7. NUMERICAL SIMULATIONS

In the numerical investigation presented in this section, the effect of liquid sloshing on the vehicle dynamics is examined. Simulations of a vehicle negotiating a curved track are performed in order to evaluate the wheel/rail contact forces and the movement of the center of mass of the tank and fluid, and to have a better understanding of the effect of liquid sloshing on vehicle dynamics when the vehicle forward velocity is varied. The traction and braking scenarios on a tangent track are also considered in order to examine the load transfer between the two trucks and the coupler forces between the two vehicles. These braking scenarios are used to evaluate the effect of liquid sloshing on the performance of the ECP brake system. The numerical results obtained in this investigation show that the liquid sloshing does not have a pronounced effect on the vehicle critical speed, but it does affect the change of the wheel load when the vehicle negotiates a curve at a velocity different from the balance speed. In the case of vehicle traction and braking, there is significant fluid motion due to the acceleration and deceleration of the vehicle. The numerical results are obtained in this section using tanks partially filled with water.

7.1 Curve Negotiation and Balance Speed Analysis

In this section, the curved track described in Table 1 is used to investigate the effect of liquid sloshing on vehicle dynamics by evaluating the wheel/rail contact forces and the movement of the center of mass of the tank and fluid when the vehicle forward velocity is varied. The track has a radius of curvature of roughly 582 m which results in a balance speed of roughly 63 km/h defined in the case of rigid body dynamics as $V = \sqrt{gRh_t/G}$, where g is the gravity constant, R is the radius of curvature of the curve, h_t is the super-elevation, and G is the track gauge. In order to examine the impact of liquid sloshing on curve negotiation, forward velocities of 40 km/h, 60 km/h, and 90 km/h are considered in this investigation.

Centrifugal Forces The effect of the centrifugal force when a vehicle is negotiating a curve is to push the vehicle outward along the direction normal to the curve. The inertia forces of the fluid can be expressed as the product of the acceleration of the center of mass and the total mass. In order to obtain the centrifugal force of the fluid and analyze its longitudinal motion, the normal and tangent vectors can be determined by using the transformation matrix of the track frame relative to the tank body [25].

Figure 11 shows the outward inertia force and the lateral component of gravity force of the fluid, which is due to the super-elevation of the track. In order to plot the curves at various velocities in one figure, the traveling time along the curve is normalized to a dimensionless parameter which represents the curve length. The results presented in this figure show that the centrifugal force exerted on the fluid is smaller than the lateral component of the gravity force when the vehicle travels below the balance speed; however, a larger centrifugal force is exerted when the vehicle speed is above the balance speed. The resultant force can affect the tank motion as shown in Fig. 12 in which the lateral displacement of the geometric center of the tank with respect to the track is plotted for both the fluid and rigid body models at various velocities. This figure illustrates that the liquid sloshing can exacerbate the unbalanced effects when the vehicle negotiates a curve at a velocity away from the balance speed. It can also be found that when the vehicle travels near the balance speed, there are no significant differences between the fluid and rigid body model since the liquid exerts the same magnitude of centrifugal force as the lateral component of gravity, as seen in Fig. 11. Traveling at a speed greater than the balance speed causes instability, which is evident by the results presented in Fig. 12c, where the oscillations of the rigid body model increase after the first curve. However, due to the damping effect of the liquid motion, the fluid model experiences increased stability compared to the rigid body model.

Figure 13 depicts the tangential component of the inertia and gravity forces at a velocity of 40 km/h, which is used to investigate the longitudinal motion of the fluid inside the tank when the vehicle is negotiating a curve. It was found that the flexible fluid experiences more than three times the tangential forces than the rigid fluid due to the liquid sloshing. Numerical simulations also show that increasing the vehicle forward velocity can increase the tangential forces applied on the fluid, which will cause larger movement in the longitudinal direction compared to the case of a lower speed, as shown in Fig. 14 in which the position of the center of mass of the liquid with respect to the tank in the longitudinal direction is plotted in various velocity cases. The results presented in this figure also show that the relative displacement increases with vehicle velocity.

Wheel/Rail Contact Forces The wheel/rail contact forces are also examined in the case of the vehicle negotiating a curve and are used to examine the impact of the liquid sloshing on wheel/rail interaction. Figures 15 and 16 depict the normal contact forces on the tread and flange, respectively, on both left and right wheels of the lead wheelset of the lead truck. The normal forces on the tread show that the liquid sloshing can intensify the load variance on both the right and left wheels, and tends to increase the amount of the load variation when the vehicle does not travel at the balance speed during the curve negotiation case. However, the normal forces on the flange increase with the vehicle forward velocity and there are no noticeable differences between the fluid and rigid body models. Figures 17 and 18 depict the lateral contact forces on the tread and flange, respectively, which exhibit similar patterns compared to the normal forces. It is clearly shown that the lateral forces on the flange increase with the vehicle forward velocity since more lateral forces are needed to balance the centrifugal forces, which also increase with the vehicle velocity.

7.2 Traction and Braking Analysis

In this investigation, motion scenarios are used to examine the impact of liquid sloshing on the vehicle nonlinear dynamics in the traction and braking cases.

Vehicle Traction Analysis In the traction scenario, a single vehicle model is used and a trajectory velocity constraint is applied on the lead stub sill to represent the vehicle traction scenario. The trajectory velocity constraint causes the vehicle to accelerate according to user-specified trajectory and velocity relationships [25]. In this investigation, a constant acceleration of 0.3 m/s^2 is used to accelerate the vehicle to 20 km/h in 15 s and then maintain this constant velocity. The average contact forces of the four wheels of the lead and rear trucks are plotted in Fig. 19. It is evident that the liquid sloshing has a significant effect on the load distribution during the vehicle traction; there is an approximately 13% difference in the normal load compared with that of the rigid body model. After traction, the liquid continues to experience sloshing towards a steady state which can be clearly seen in Fig. 20, which shows the longitudinal displacement of the fluid center of mass with respect to the tank during the traction. It is apparent that there is a maximum motion of roughly 0.7 m of the center of mass, which will certainly affect the wheel load as shown in Fig. 19.

Vehicle Braking Analysis In order to consider the coupler force between cars, a two tank-car model is developed based on the single MBS vehicle model to simulate the braking scenarios, in which the coupler is represented as a linear spring-damper force element. The nonlinear braking torque associated with the vehicle loads and forward velocities is applied on the wheelsets to perform braking in this analysis. The case where only the lead car brakes as well as the case where both cars brake are simulated in order to consider the usual brake situations. These two scenarios are used to examine the effects of liquid sloshing on the dynamic response of the train during braking when the conventional and ECP brake systems are used. In this investigation, the train is decelerated from 40 km/h to 5 km/h in 40s with a nonlinear braking force. The coupler used in this model has a stiffness coefficient 300 $\mathrm{MN/m}$ and a damping coefficient of 200 $\mathrm{kN{\cdot}s/m}$. The coupler forces are plotted in Fig. 21 in the case where only the lead car brakes as well as the case of both cars braking, for both the fluid and rigid body models. By comparing the results in Figs. 21a and 21b, it can be seen that a larger coupler force is exerted when only the lead car brakes regardless of whether the flexible fluid or the equivalent rigid fluid model is used, which shows the significance of ECP application in railroad vehicles. In the case of brake application on the lead car only, the flexible fluid model has essentially the same coupler force as that of the rigid fluid model initially, while it experiences a larger value as the vehicle velocity decreases. However, in the case of uniform and simultaneous brake application on both cars (ECP), the flexible fluid model shows significantly larger coupler forces than the rigid body model for the entire scenario due to the increased relative motion of the fluid inside the tank as shown in Fig. 22, which depicts the longitudinal and lateral displacement of the center of mass of the fluid with respect to the tank. It is clearly shown that in the case of ECP braking, the fluid moves more significantly because the vehicle system experiences a more severe acceleration resulting from increased braking torques that are applied as compared to the conventional brake scenario. Figure 23 shows the configuration of these two cars partially filled with water in braking, and it can be clearly seen that there is significant liquid motion due to the deceleration of the vehicle.

8. SUMMARY AND CONCLUSIONS

In this paper, a new approach is proposed for the integration of a continuum-based sloshing model with a fully nonlinear MBS rail vehicle model. The contributions of this paper are as follows: (1) In this investigation, a unified geometry/analysis mesh is used from the outset in order to accurately capture complex fluid and tank geometries as well as the nonlinear dynamic behavior of the fluid and vehicle. The approach developed in this study is used to examine the effects of liquid sloshing on vehicle dynamics when negotiating a curve and during traction or braking; (2) The method of the tank and fluid geometry description is introduced and it is shown how a unified geometry/analysis mesh can be developed for both the rigid rail and continuum fluid bodies. The search method used to define the fluid/tank contact points is outlined and the penalty force model used to describe the fluid/tank interaction forces is formulated; (3) The fluid constitutive equations that account for the viscosity and incompressibility effects are presented. The liquid sloshing model developed in this study is integrated with the MBS railroad vehicle model which takes into consideration the nonlinear three-dimensional wheel/rail contact forces and the wheel and rail profile geometries; and (4) In order to systematically examine the effect of the motion of the flexible fluid on vehicle dynamics when the vehicle is negotiating a curve, a general definition of the outward inertia force of a flexible body using both FFR and ANCF descriptions is investigated. The analysis presented in this study shows that this force depends strongly on the motion of the continuum and does not take the simple form used in the case of rigid body dynamics.

Comparative simulations are performed to examine the liquid sloshing effects by using flexible and rigid body fluid models. It is shown that the liquid sloshing can exacerbate the unbalanced effects when the vehicle travels at a velocity away from the balance speed, but this effect decreases when the forward velocity is close to the balance speed because the liquid experiences the same centrifugal force as the rigid fluid body in this case. The results in the traction analysis show that the liquid motion can significantly affect the load distribution between the front and rear trucks. Comparing with the ECP braking case, there is a larger coupler force when the conventional braking is used for both the flexible and rigid body fluid models. Nonetheless, the results obtained for the model considered in this investigation demonstrate that the liquid sloshing amplifies the coupler force greatly in the ECP braking case compared to the equivalent rigid body model because the latter model cannot capture the fluid nonlinear inertia effects.

Acknowledgements

This research was supported by the National Science Foundation (Project # 1632302) and, in part, by the scholarship under the State Scholarship Fund organized by the China Scholarship Council (CSC) in 2014, and by the projects of the National Natural Science Foundation of China (Grant No. U1334206; No. 51475388).

REFERENCES

1. Abramson, H.N., 1966, “The dynamic behavior of liquids in moving containers, with applications to space vehicle technology”, NASA SP-106.
2. Aboubakr, A.K., Volpi, M., Shabana, A.A., Cheli, F. and Melzi, S., 2016, “Implementation of electronically controlled pneumatic brake formulation in longitudinal train dynamics algorithms”. *Proceedings of the Institution of Mechanical Engineers, Part K: Journal of Multi-body Dynamics*, online first, DOI: 1464419316628764.
3. Aboubakr, A. K., and Shabana, A. A., 2015, “Efficient and Robust Implementation of the TLISMNI Method”, *Journal of Sound and Vibration*, 353, pp. 220-242.
4. Aliabadi, S., Johnson, A. and Abedi, J., 2003, “Comparison of finite element and pendulum models for simulation of sloshing”. *Computers & Fluids*, 32(4), p.535-545.
5. Akyildız, H. and Ünal, N.E., 2006, “Sloshing in a three-dimensional rectangular tank: numerical simulation and experimental validation”. *Ocean Engineering*, 33(16), pp.2135-2149.
6. Bogomaz, G. I., Markova, O. M., and Chernomashentseva, Y. G, 1998, “Mathematical modelling of vibrations and loading of railway tanks taking into account the liquid cargo mobility”. *Vehicle System Dynamics*, 30(3-4), p.285-294.
7. Cottrell, J.A., Hughes, T.J.R., and Reali, A., 2007, “Studies of Refinement and Continuity in the Isogeometric Analysis”, *Comput. Methods in Appl. Mech. Engrg.* Vol. 196, pp. 4160-4183.
8. Delorme, L., Colagrossi, A., Souto-Iglesias, A., Zamora-Rodriguez, R. and Botia-Vera, E., 2009, “A set of canonical problems in sloshing, Part I: pressure field in forced roll comparison between experimental results and SPH”. *Ocean Engineering*, 36, pp.168-178.

9. Faltinsen, O.M., 1974, “A nonlinear theory of sloshing in rectangular tanks”, *Journal of Ship Research*, 18(4), pp. 224-241.
10. Gialleonardo, E. D., Premoli, A., Gallazzi, S. and Bruni, S., 2013, “Sloshing effects and running safety in railway freight vehicles”. *Vehicle System Dynamics*, 51(10), p.1640-1654.
11. Ibrahim, R.A., Pilipchuk, V.N. and Ikeda, T., 2001, “Recent advances in liquid sloshing dynamics”. *Applied Mechanics Reviews*, 54(2), pp.133-199.
12. Kalker, J.J., 1990, *Three-Dimensional Elastic Bodies in Rolling Contact*, Kluwer Academic Publishers, Dordrecht, The Netherlands.
13. King, C. and Trichur, R., 2015, *Train carrying crude oil derails in Ontario*. WSJ, http://www.wsj.com/articles/train-carrying-crude-oil-derails-in-ontario-1424015961.
14. Love, J.S. and Tait, M.J., 2011, “Equivalent linearized mechanical model for tuned liquid dampers of arbitrary tank shape”. *Journal of Fluids Engineering*, 133(6), p.061105.
15. Moiseyev, N.N. and V.V. Rumyantsev., 1968, *Dynamic Stability of Bodies Containing Fluid*, Springer-Verlag, Berlin, Heidelberg.
16. Olshevskiy, A., Dmitrochenko, O. and Kim, C.W., 2014, “Three-Dimensional Solid Brick Element Using Slopes in the Absolute Nodal Coordinate Formulation”. *Journal of Computational and Nonlinear Dynamics*, 9(2), p.021001.
17. Petravic, J., 2007, “On the equilibrium calculation of the friction coefficient for liquid slip against a wall,” *Journal of Chemical Physics*, Vol. 127.
18. Piegl. L., Tiller. W., 1997, *The NURBS Book*, Second Edition, Springer, New York.
19. Pit, R., Hervet H., Leger, L., 1999, “Friction and slip of a simple liquid at a solid surface,” *Tribology Letters*, pp. 147-152.

20. Ranganathan, R., Ying, Y. and Miles, J. B., 1993, “Analysis of fluid slosh in partially filled tanks and their impact on the directional response of tank vehicles”, *SAE Technical Paper*, No. 932942.

21. Ranganathan, R., Ying, Y. and Miles, J.B., 1994, “Development of a mechanical analogy model to predict the dynamic behavior of liquids in partially filled tank vehicles”, *SAE Technical Paper*, No. 942307.

22. Rebouillat, S. and Liksonov, D., 2010, “Fluid–structure interaction in partially filled liquid containers: a comparative review of numerical approaches”. *Computers and Fluids*, 39(5), pp.739-746.

23. Sanborn, G., Tobaa, M. and Shabana, A. A., 2008, “Coupling between structural deformations and wheel-rail contact geometry in railroad vehicle dynamics”. *Proceedings of the Institution of Mechanical Engineers, Part K: Journal of Multi-body Dynamics*, 222(4), p.381-392.

24. Shabana, A. A., Tobaa, M., Sugiyama, H. and Zaazaa, K., 2005. “On the Computer Formulations of the Wheel/Rail Contact Problem”. *Nonlinear Dynamics*, 40(2), p.169-193.

25. Shabana, A. A., Zaazaa, K. E., and Sugiyama, H., 2008, *Railroad Vehicle Dynamics*: *A Computational Approach*, Taylor & Francis/CRC, Boca Raton, FL.

26. Shabana, A. A., 2017, *Computational Continuum Mechanics*, 3rd ed., Cambridge University, Cambridge, UK.

27. Shabana, A. A., 2013, *Dynamics of Multibody Systems*, 4th ed., Cambridge University, New York.

28. Shi, H., Wang, L. and Shabana, A. A., 2016, “Dynamics of flexible body negotiating a Curve”, *Journal of Computational and Nonlinear Dynamics*, 11(4), p.041020.

29. Spencer, A. J. M., 1980, *Continuum Mechanics*, Longman, London, England.

30. Vera, C., Paulin, J., Suarez, B. and Gutiérrez, M., 2005, "Simulation of freight trains equipped with partially filled tank containers and related resonance phenomenon". *Proceedings of the Institution of Mechanical Engineers, Part F: Journal of Rail and Rapid Transit*, 219(4), p. 245-259.

31. Wang, L., Jimenez-Octavio, J. R., Wei, C. and Shabana, A. A., 2014, "Low Order Continuum-Based Liquid Sloshing Formulation for Vehicle System Dynamics", *Journal of Computational and Nonlinear Dynamics*, 10(2), p.021022.

32. Wang, L., Shi, H. and Shabana, A. A., 2016, "Effect of the tank-car thickness on the nonlinear dynamics of railroad vehicles". *Proceedings of the Institution of Mechanical Engineers, Part K: Journal of Multi-body Dynamics*, DOI: 10.1177/1464419316642930.

33. Wei, C., Wang, L. and Shabana, A.A., 2015, "A total Lagrangian ANCF liquid sloshing approach for multibody system applications". *Journal of Computational and Nonlinear Dynamics*, 10(5), p.051014.

34. White, F. M., 2011, *Fluid Mechanics*, 4th edition, The McGraw-Hill Companies, Inc., New York.

35. Wronski R., 2013, *As more oil flows by rail, concerns grow about safety of the tank-cars*. tribunedigital-chicagotribune, http://articles.chicagotribune.com/2013-11-29/news/ct-dangerous-tank-cars-met-1129-20131129_1_tank-cars-oil-production-more-oil-flows.

Nomenclature

$\mathbf{A}^i$	Transformation matrix for an FFR body i
$\mathbf{C}_r^j$	Right Cauchy-Green deformation tensor of an ANCF element j
$\mathbf{D}^j$	Rate of deformation tensor of an ANCF element j
$\mathbf{e}^{ij}$	Vector of ANCF nodal coordinates of element j on body i defined in the current configuration
$\mathbf{e}_o$	Vector of ANCF nodal coordinates defined in the reference configuration
f_n	Normal contact force between fluid and tank wall
f_t	Tangential friction force between fluid and tank wall
F^i	Outward inertia force body i
$\mathbf{f}_p$	Penalty force vector
g	Gravity constant
G	Track gauge
h	Height of fluid free surface
h_t	Track superelevation
$\mathbf{J}_o$	Jacobian matrix of the position vector gradients; $\mathbf{J}_o = \partial \mathbf{X} / \partial \mathbf{x}$
$\mathbf{J}$	Jacobian matrix of the position vector gradients; $\mathbf{J} = \partial \mathbf{r} / \partial \mathbf{X}$
$\mathbf{J}_e$	Jacobian matrix of the position vector gradients; $\mathbf{J}_e = \partial \mathbf{r} / \partial \mathbf{x}$
K, C	Penalty coefficients for fluid/tank contact at the position, velocity levels
L	Tank length
m	Mass of a rigid body
m^i	Mass of a flexible body i
m^{ij}	Mass of an ANCF element j on body i

$\mathbf{m}^{j}$ Mass matrix of an ANCF element j

$\mathbf{m}^{ij}$ Mass matrix of an ANCF element j on body i

$\mathbf{M}_{e}$ Mass matrix of an ANCF body

$\mathbf{M}_{r}$ Mass matrix of a rigid body

$\mathbf{n}$ Unit normal vector to curve

$\mathbf{n}^{ij}$ Unit normal vector to ANCF rail element j on body i

$\hat{\mathbf{n}}_{P}^{t}$ Unit normal vector at contact point P in tank

$\mathbf{q}_{r}^{i}$ FFR body i reference coordinates

$\mathbf{q}_{r}$ Rigid body reference coordinates

$\mathbf{q}_{f}^{i}$ FFR body i elastic coordinates

$\mathbf{Q}_{P}^{fj}$ Generalized contact forces on point P on ANCF element j on fluid body f

$\mathbf{Q}_{P}^{t}$ Generalized contact forces on point P associated with the tank coordinates

$\mathbf{Q}_{v}^{j}$ Generalized viscous forces on ANCF element j

$\mathbf{Q}_{e}$ Generalized external and elastic forces on an ANCF body

$\mathbf{Q}_{e}^{j}$ Generalized external forces on ANCF element j

$\mathbf{Q}_{s}^{j}$ Generalized elastic forces on ANCF element j

$\mathbf{Q}_{r}$ Generalized forces associated with the rigid coordinates

$\mathbf{Q}_{d}$ Quadratic velocity vector

$\mathbf{Q}_{IC}^{j}, \mathbf{Q}_{TD}^{j}$ Generalized penalty forces on ANCF element j

r Radius of tank

$\mathbf{r}^{i}$ Position vector to an arbitrary point on an FFR body i

$\mathbf{r}_c^i$ Position vector to the center of mass of an ANCF body

$\mathbf{r}^{ij}$ Position vector to an arbitrary point on an ANCF element j on body i

$\mathbf{r}_\alpha^{ijk}$ Gradient vector at node k of an ANCF element j on body i

R Radius of curve

$\mathbf{R}^i$ FFR body i reference translation

s^i Arc length traveled by body i

s^r Rail surface parameters

s^w Wheel surface parameters

$\mathbf{S}^i$ Shape function matrix for an FFR body i

$\mathbf{S}^{ij}$ Shape function matrix for an ANCF element j in body i

$\mathbf{t}_P^t$ Unit tangent vector at contact point P in tank

$\mathbf{t}_l^k$ Wheel/rail contact point tangent vectors

$\bar{\mathbf{u}}^i$ Local position vector of an arbitrary point on an FFR body i

$\bar{\mathbf{u}}_o^i$ Local position vector in the undeformed state on an FFR body i

$\bar{\mathbf{u}}_f^i$ Local deformation vector on an FFR body i

U_{IC}^j, U_{TD}^j Strain energy and dissipation penalty functions on ANCF element j

V Volume of an ANCF body in the straight configuration, or the forward velocity of a rigid body

V^i Volume of a flexible body i

V^{ij} Volume of an ANCF element j on body i

V_o Volume of an ANCF body in the curved reference configuration

v Volume of an ANCF body in the current configuration

$\mathbf{v}_{Pr}^{ft}$ Relative velocity vector at contact point P between the fluid body f and the tank body t

$x_c^t y_c^t z_c^t$ Coordinate system of cylindrical section of tank

$x_e^t y_e^t z_e^t$ Coordinate system of ellipsoidal section of tank

Greek Symbols

δ Relative interpenetration between fluid/tank or wheel/rail

δW_e^j Virtual work of the external forces of an ANCF element j

δW_i^j Virtual work of the inertia forces of an ANCF element j

δW_v^j Virtual work of the fluid viscosity forces of an ANCF element j

$\boldsymbol{\varepsilon}^j$ Green-Lagrangian strain tensor of an ANCF element j

$\boldsymbol{\lambda}$ Vector of Lagrange multipliers

μ Coefficient of friction between fluid and tank wall

μ_f Coefficient of shear viscosity

ρ^i Mass density of a flexible body i

ρ^{ij} Mass density of an ANCF element j on body i

$\boldsymbol{\sigma}^j$ Cauchy stress tensor of an ANCF element j

$\boldsymbol{\sigma}_{P2}^j$ Second Piola-Kirchoff stress tensor of an ANCF element j

θ^i Reference orientation of an FFR body i

$\boldsymbol{\omega}^t$ Angular velocity vector of tank body t

List of Figure Captions

Rigid-Lead, Fluid-Lead, Rigid-Rear, Fluid-Rear)

Figure 20. Fluid center of mass longitudinal displacement with respect to the tank in the traction case.

Figure 21. Coupler forces between two cars in the case of braking. (a) Conventional brake, (b) ECP brake. (Rigid, Fluid)

Figure 22. Front car fluid center of mass displacement with respect to the tank during braking. (a) Longitudinal, (b) Lateral direction. (Conventional brake, ECP brake)

Figure 23. Braking animation of two tank-cars filled with liquid. (a) Parked state, (b) Braking state.

Table 1. Track Geometry

Segment Points No.	Distance (ft)	Curvature (Deg.)	Super-elevation (in)	Grade (%)	Right rail cant angle (rad)	Left rail cant angle (rad)
A	0	0	0	0	0.025	-0.025
B	100	0	0	0	0.025	-0.025
C	300	3	3	0	0.025	-0.025
D	600	3	3	0	0.025	-0.025
E	800	0	0	0	0.025	-0.025
F	1000	0	0	0	0.025	-0.025
G	1200	-3	-3	0	0.025	-0.025
H	1500	-3	-3	0	0.025	-0.025
I	1700	0	0	0	0.025	-0.025
J	2800	0	0	0	0.025	-0.025

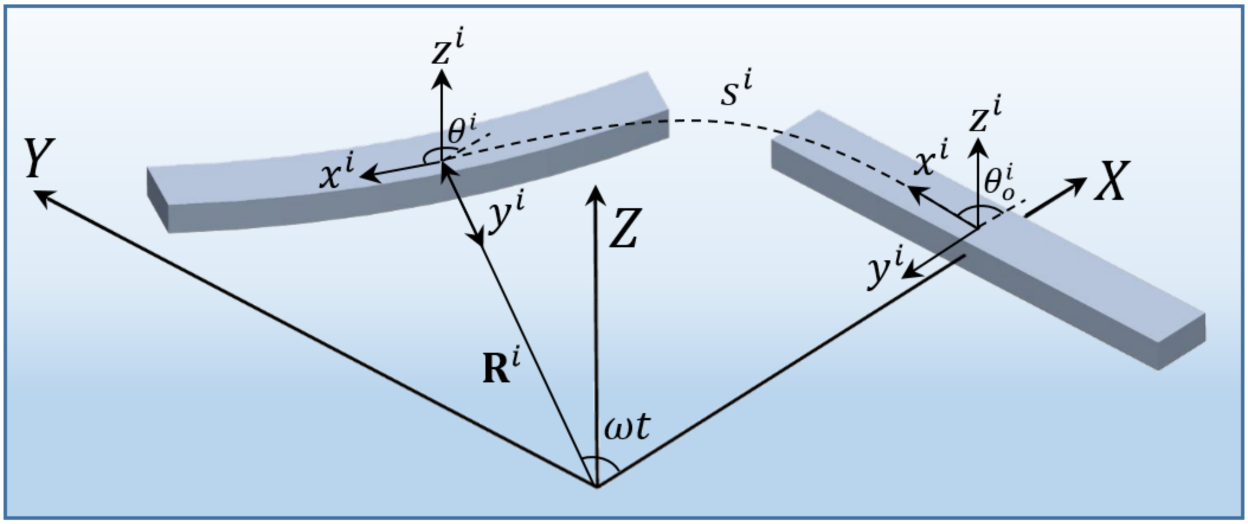

Figure 1. A planar flexible body negotiating a curve

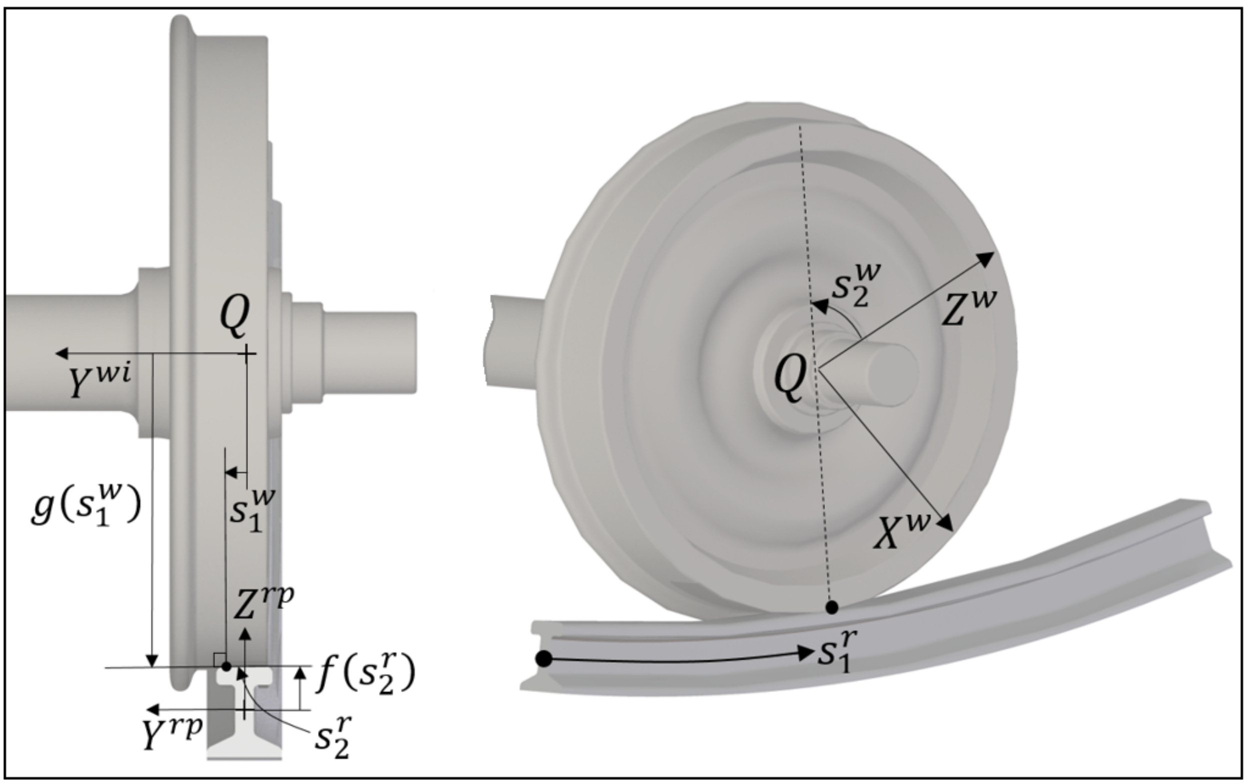

Figure 2. Wheel/rail contact.

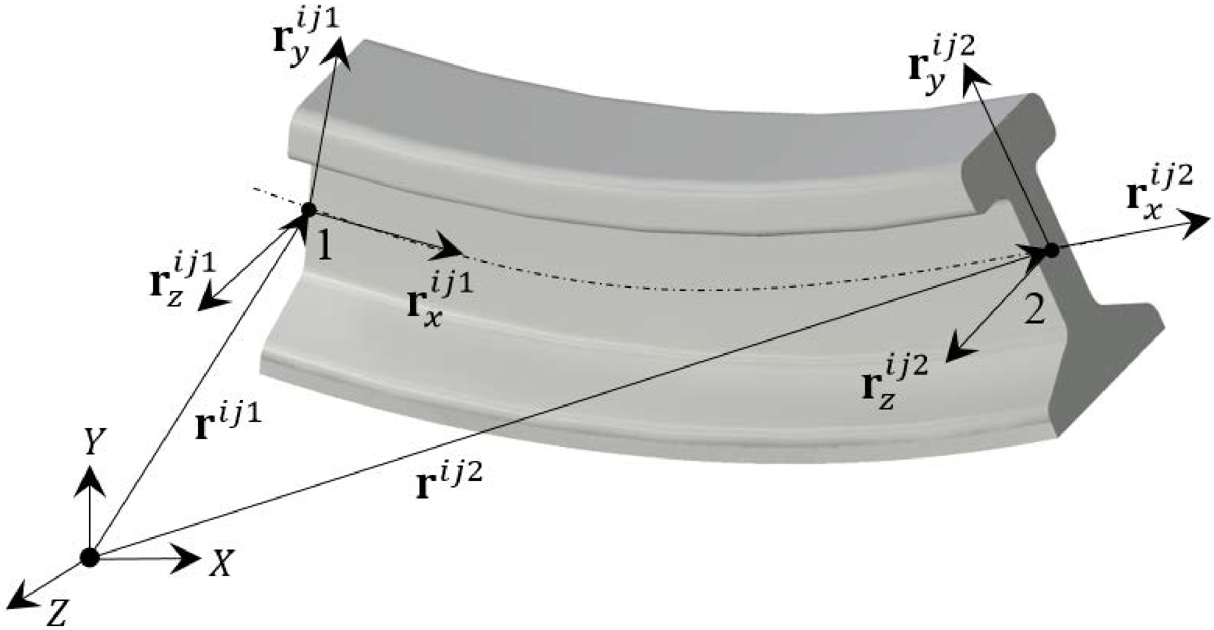

Figure 3. Curved ANCF rail element.

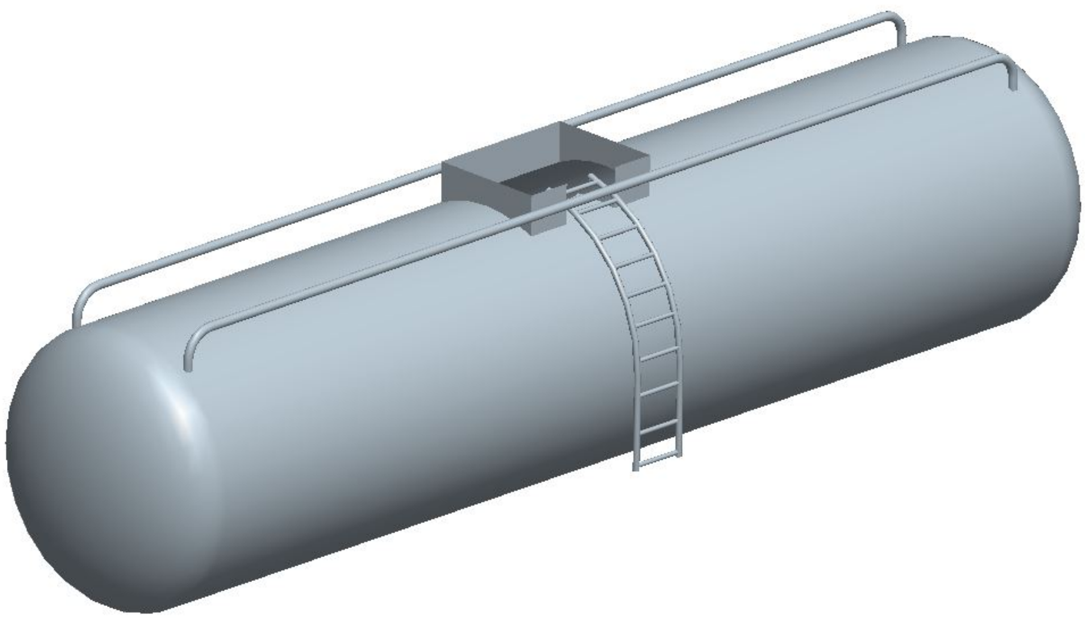

Figure 4. Fluid and tank geometry.

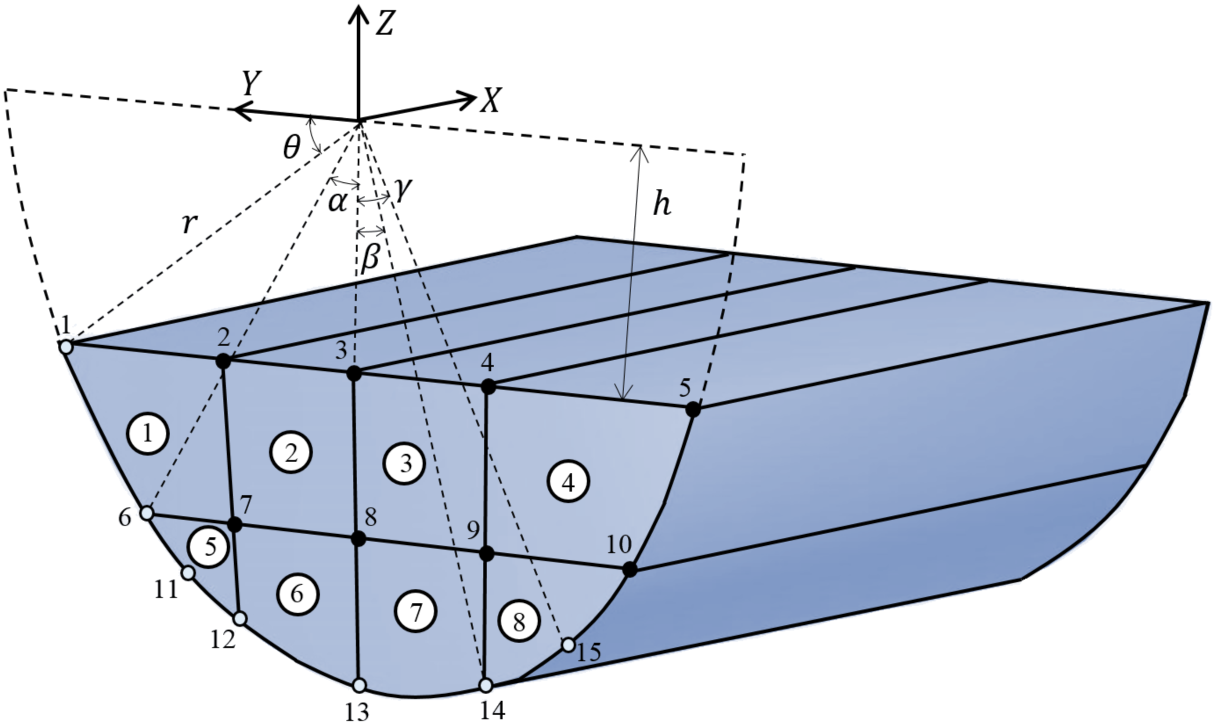

Figure 5. Cross-section mesh of the fluid inside a cylindrical tank.

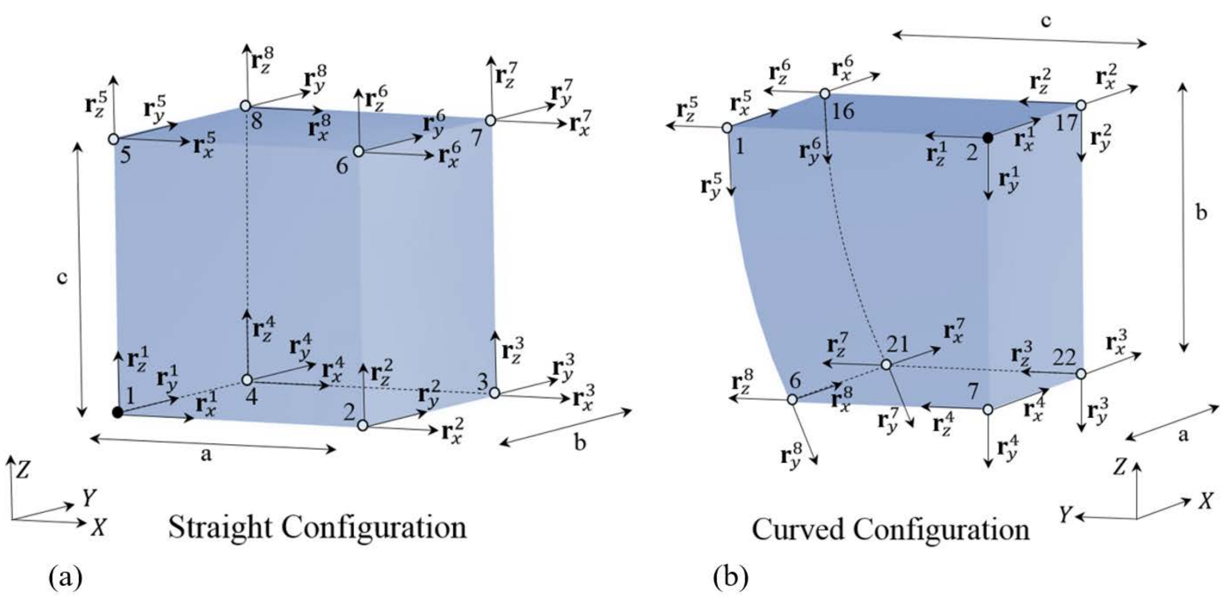

Figure 6. ANCF solid element in the (a) curved reference and (b) straight configurations.

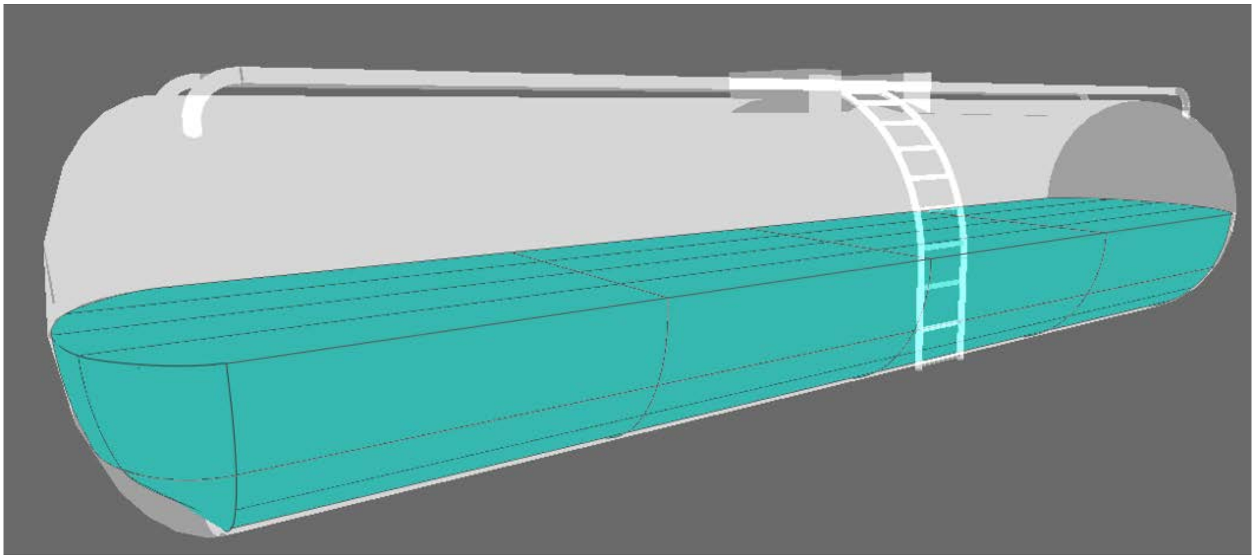

Figure 7. Initially curved ANCF fluid mesh.

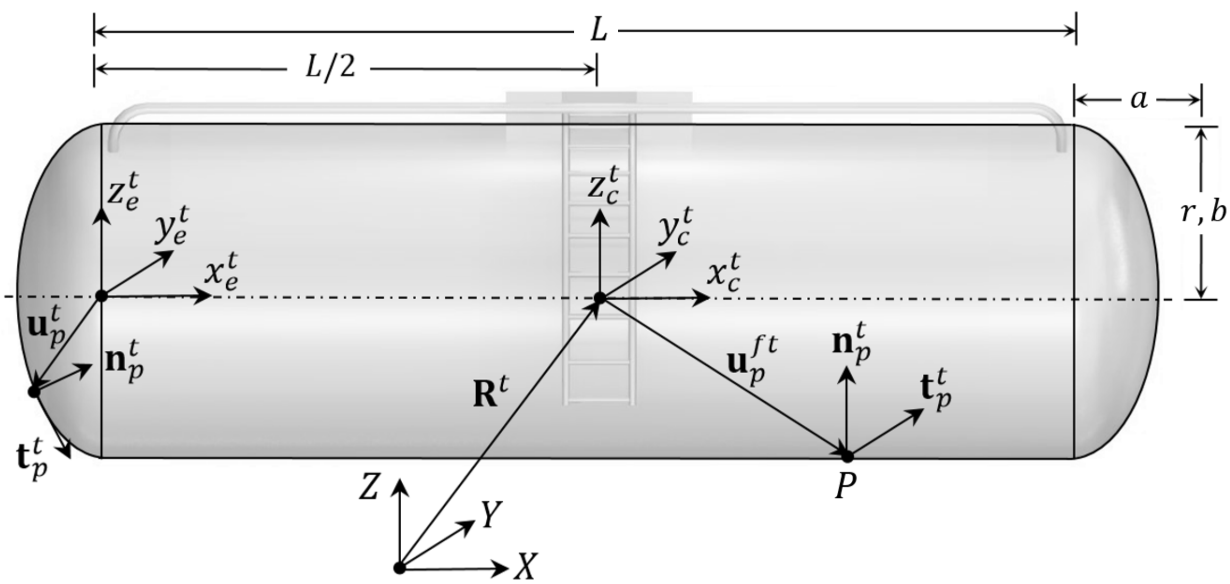

Figure 8. Tank geometry and coordinate systems.

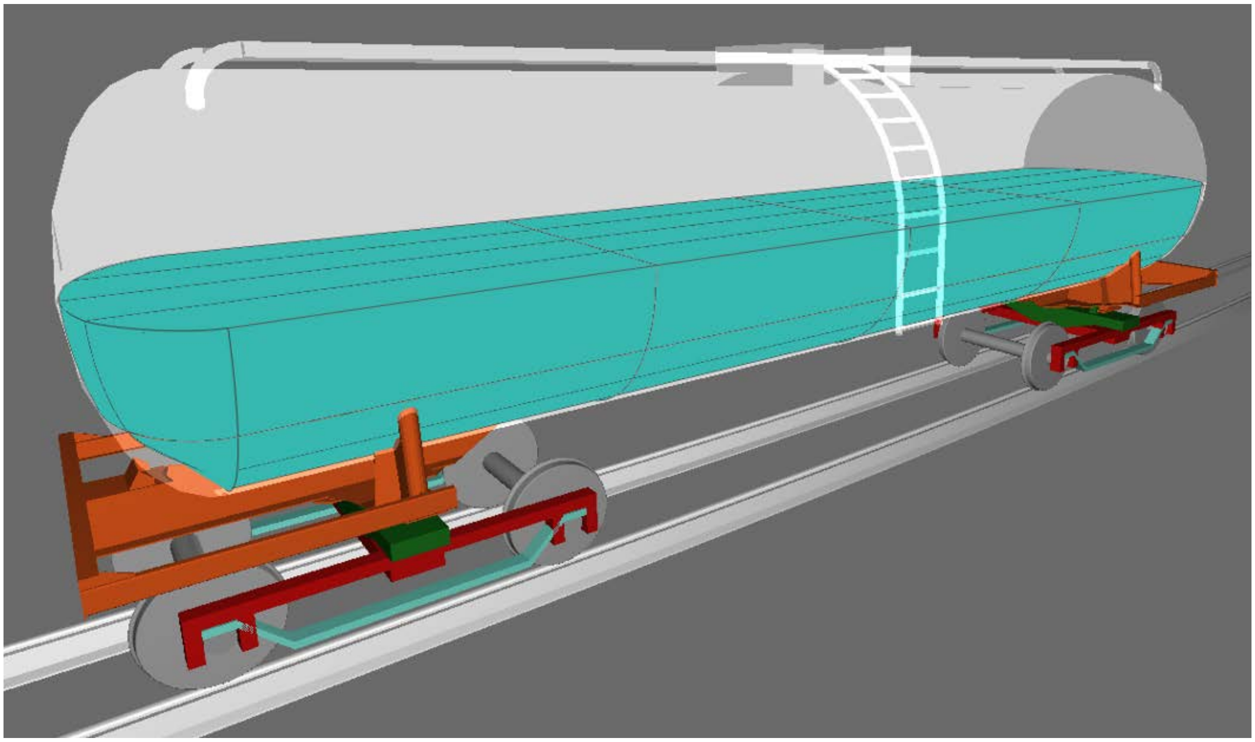

Figure 9. Railroad vehicle model.

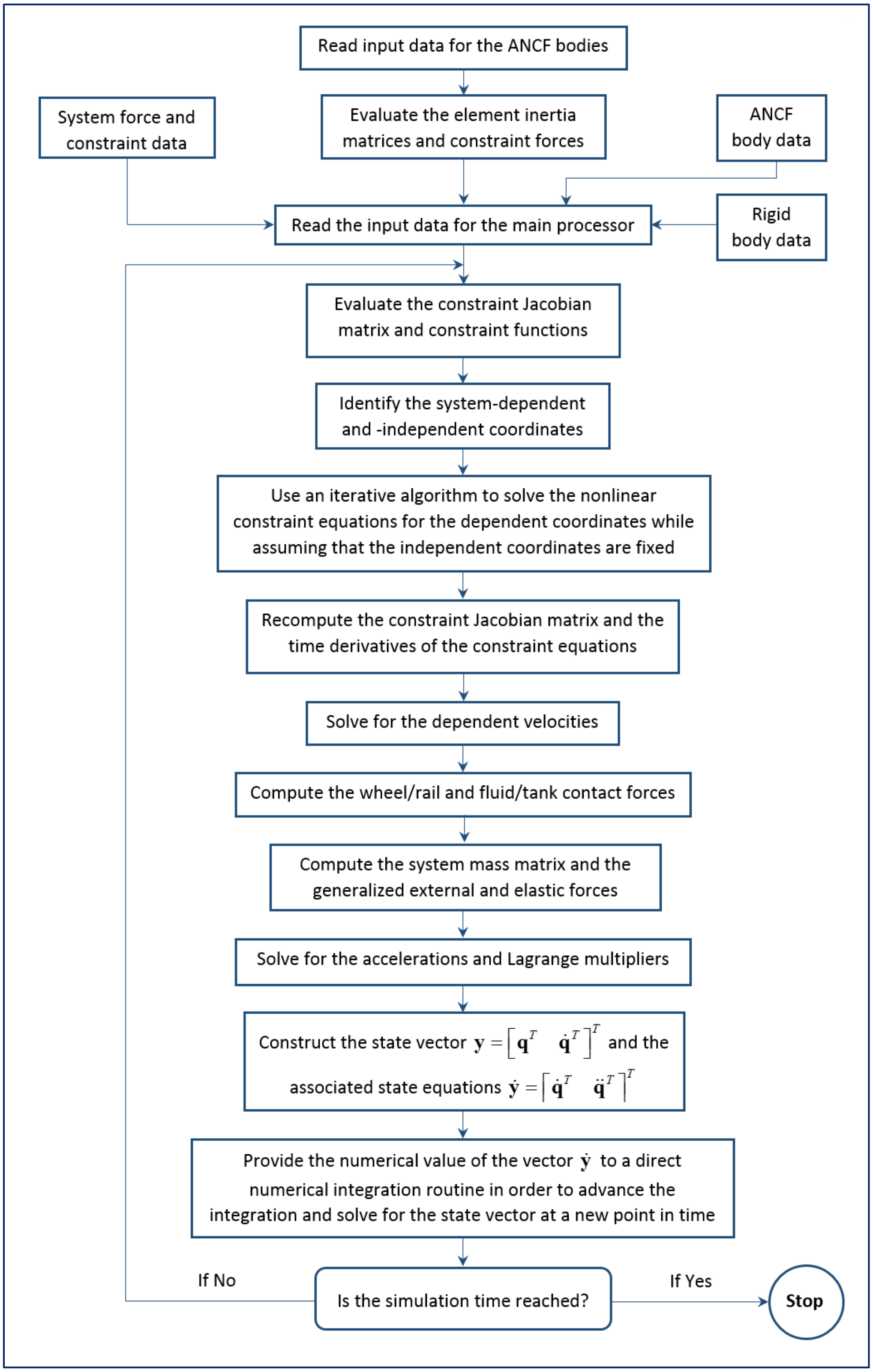

Figure 10. Flowchart of the numerical solution procedure

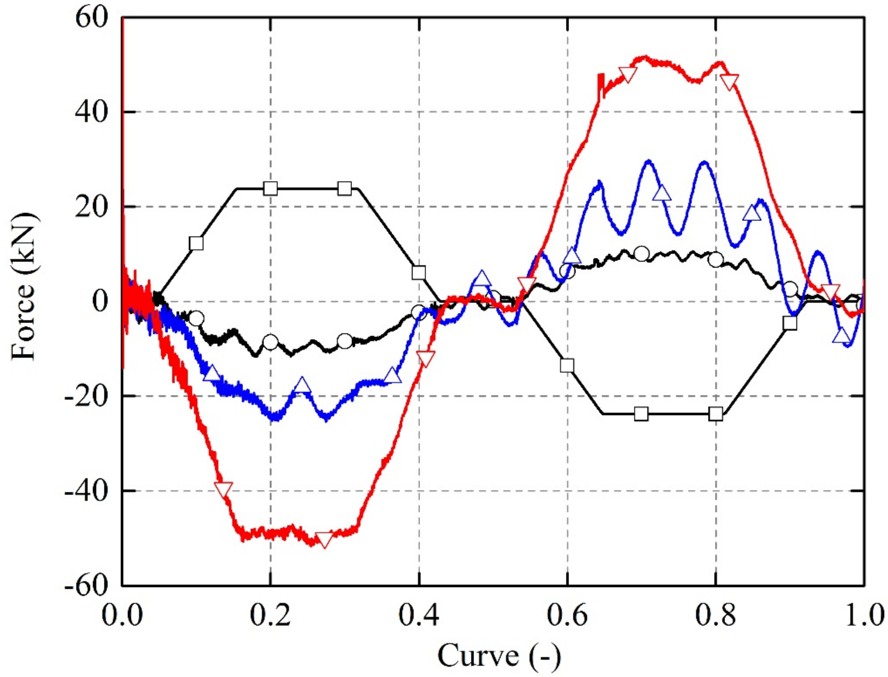

Figure 11. Lateral component of gravity and outward inertia forces of the fluid. (—□—Gravity force, —○—40km/h, —△—60km/h, —▽—90 km/h)

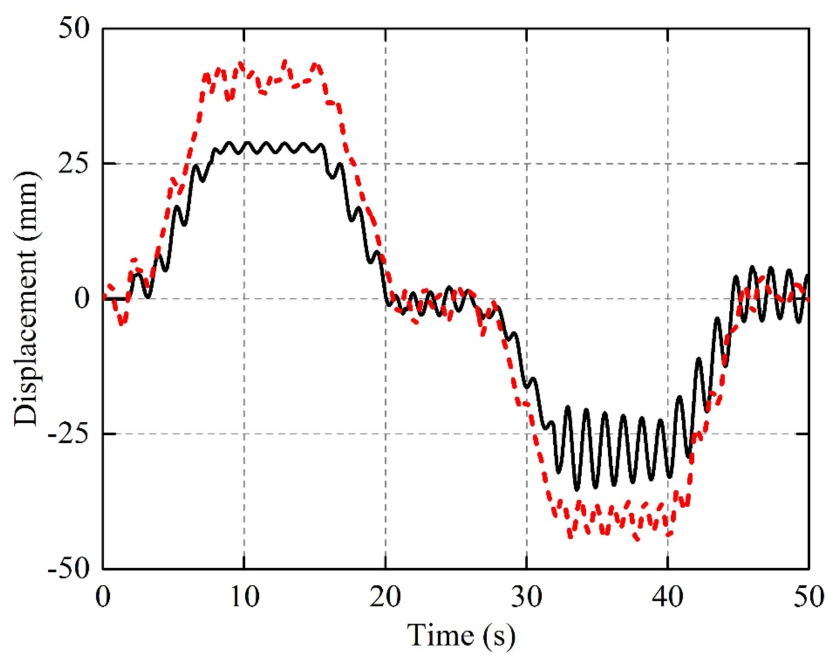

(a)

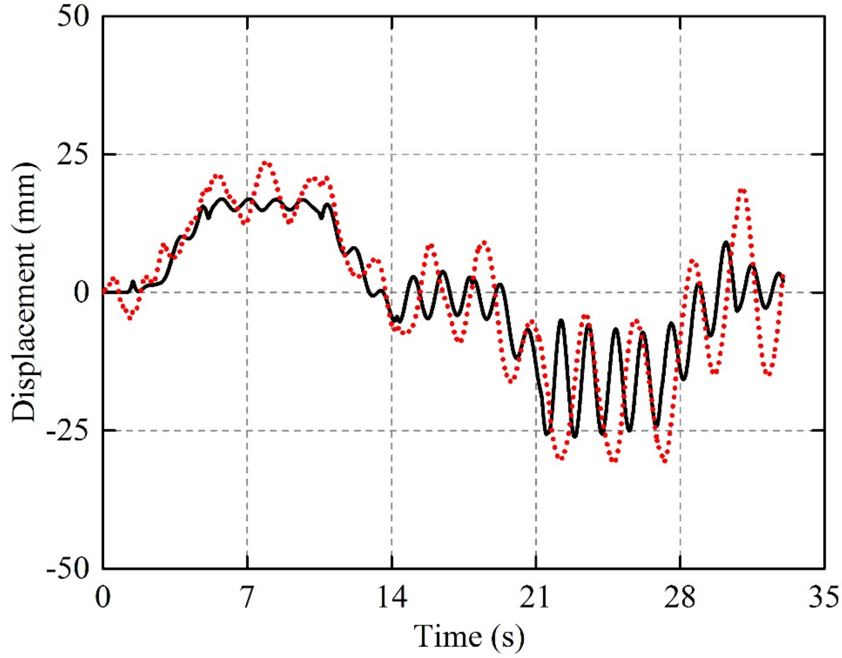

(b)

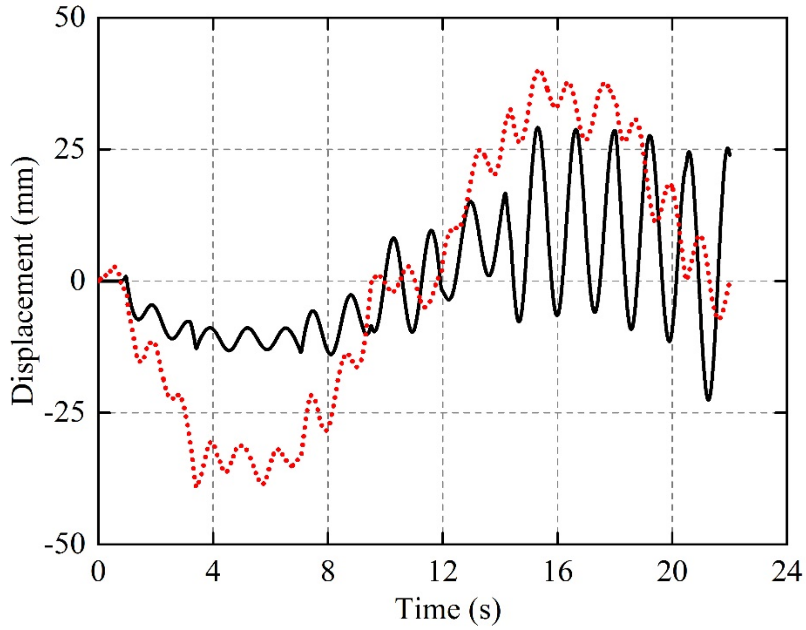

(c)

Figure 12. Position of the tank center with respect to the track in the lateral direction for different velocities. (a) 40km/h, (b) 60 km/h, (c) 90 km/h. (——Rigid, ·········Fluid)

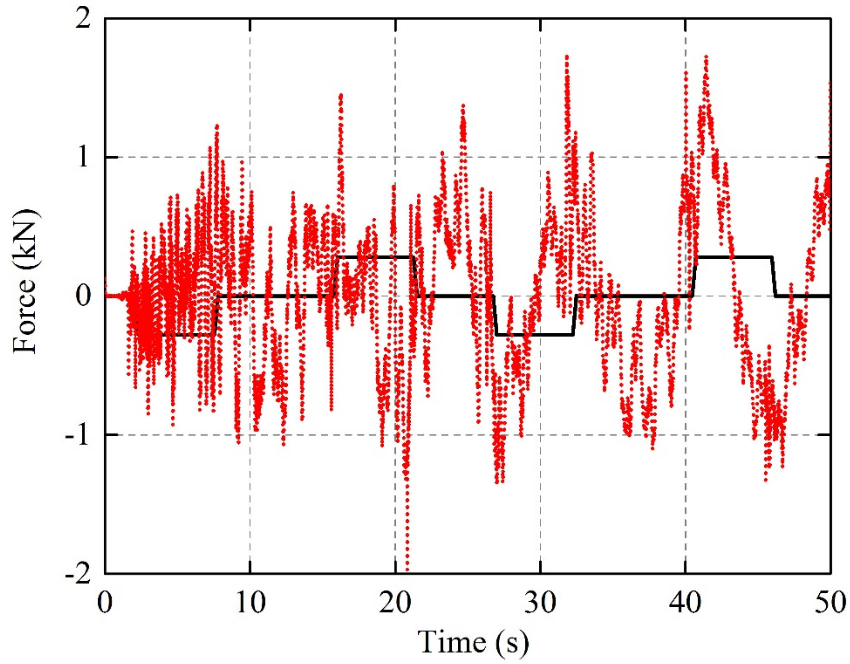

Figure 13. Tangential component of fluid gravity and inertia forces at 40 km/h. (——Gravity force, ········Inertia force)

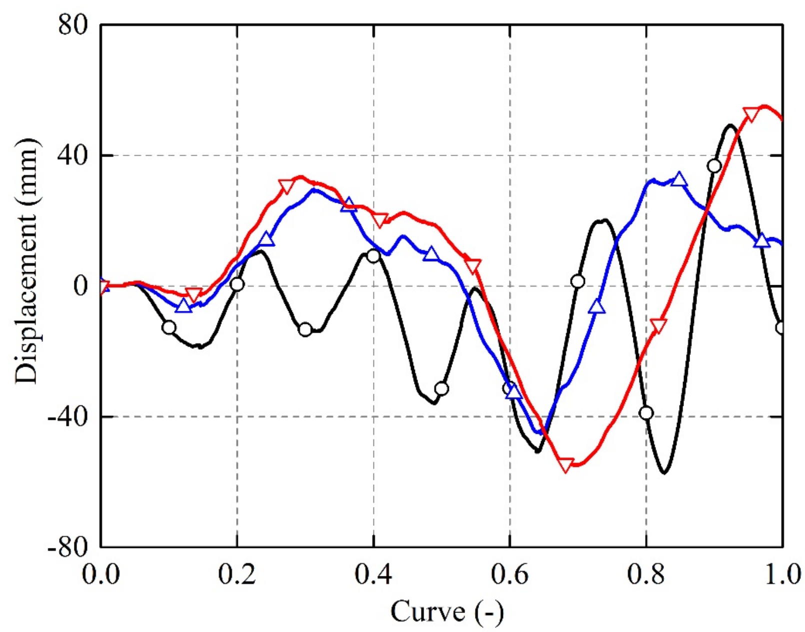

Figure 14. Liquid center of mass with respect to the tank in the longitudinal direction. (—○— 40km/h, —△—60km/h, —▽—90 km/h)

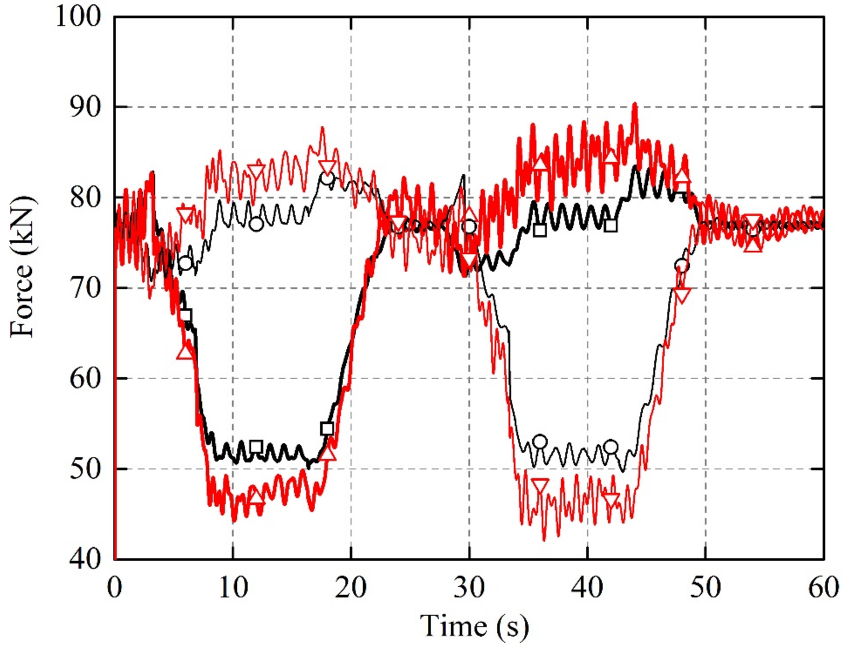

100
90
80
70
60
50
40
Force (kN)
0
10
20
30
40
50
60
Time (s)

(a)

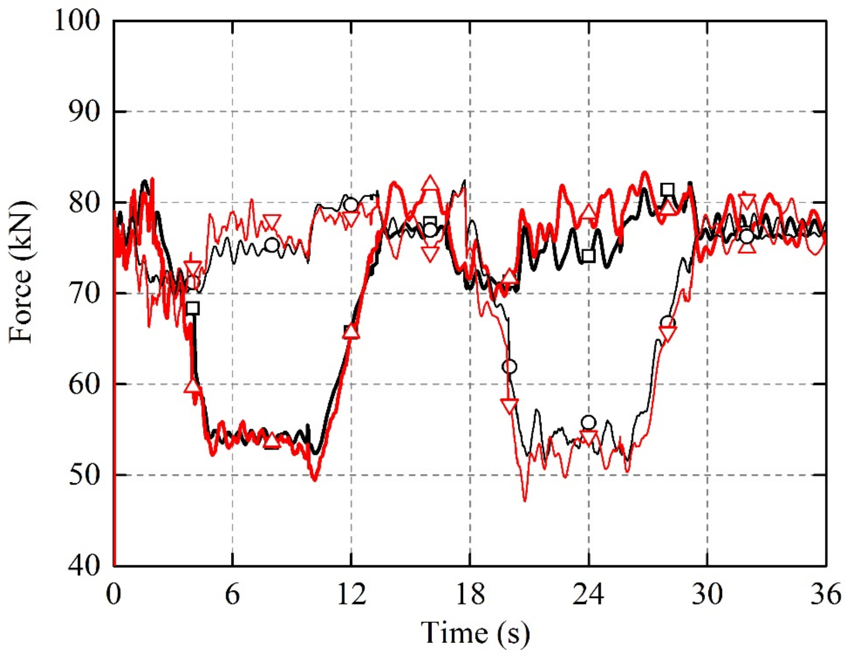

100
90
80
70
60
50
40
Force (kN)
0
6
12
18
24
30
36
Time (s)

(b)

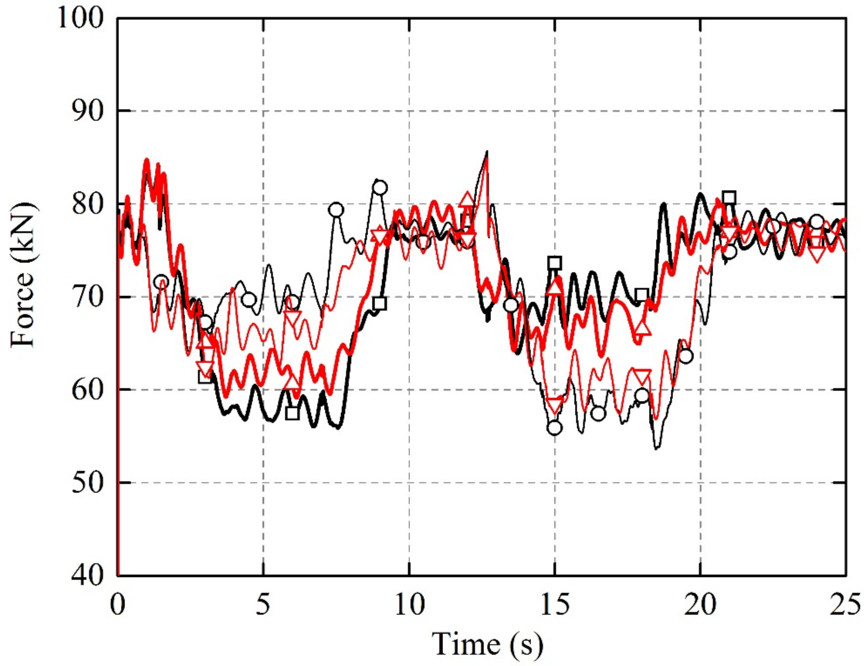

(c)

Figure 15. Tread normal contact force of truck lead wheelset. (a) 40km/h, (b) 60 km/h, (c) 90 km/h. (Rigid-Right, Fluid-Right, Rigid-Left, Fluid-Left)

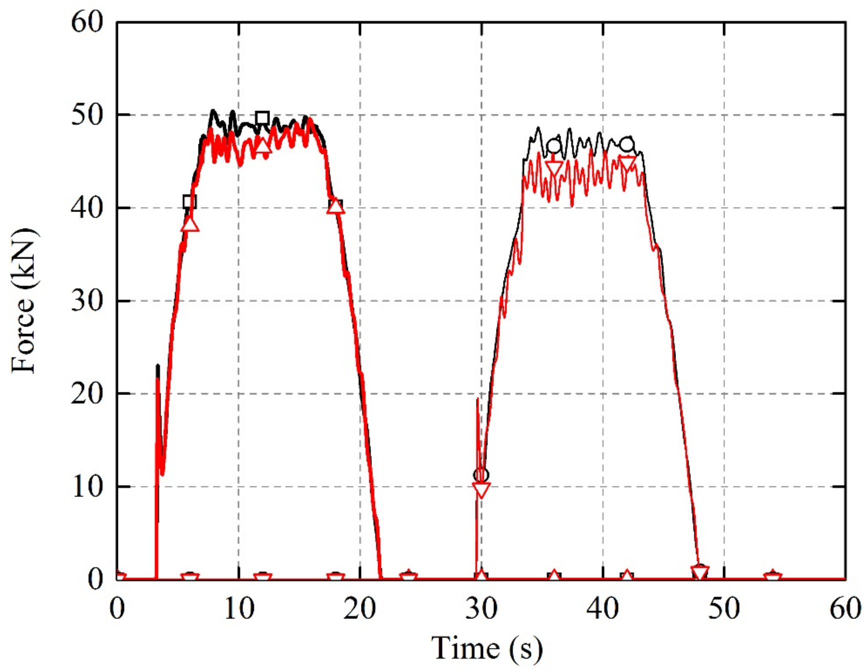

(a)

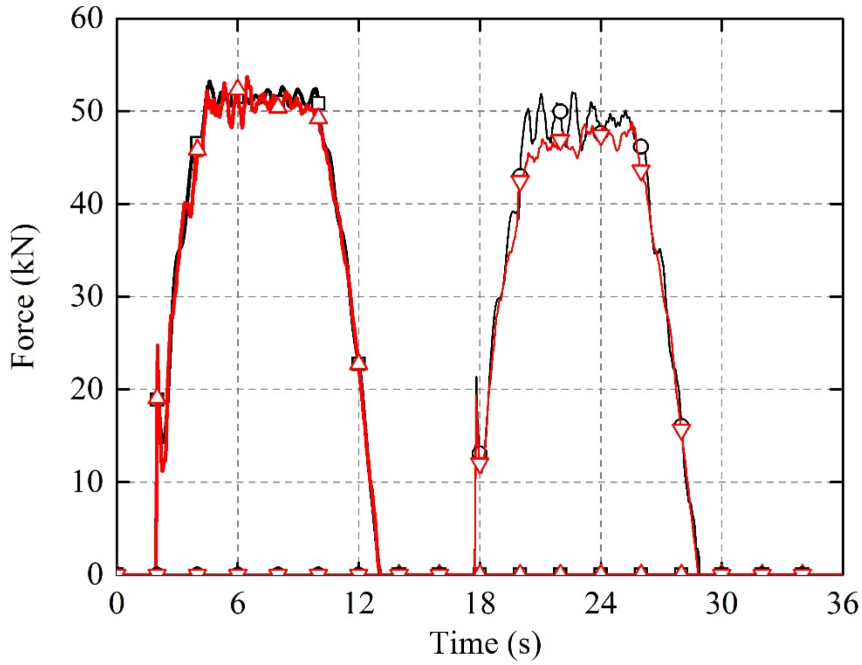

(b)

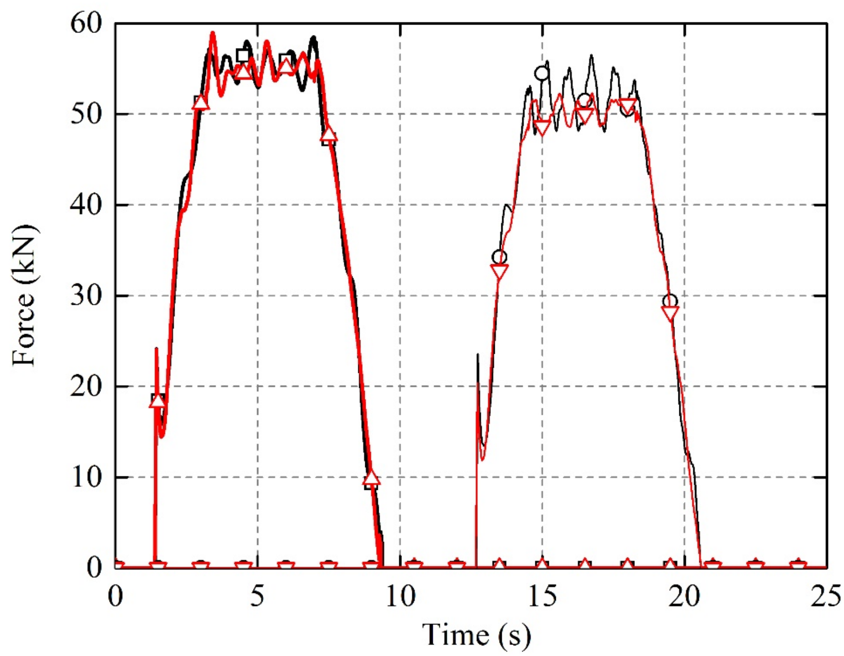

(c)

Figure 16. Flange normal contact force of truck lead wheelset. (a) 40km/h, (b) 60 km/h, (c) 90 km/h. (Rigid-Right, Fluid-Right, Rigid-Left, Fluid-Left)

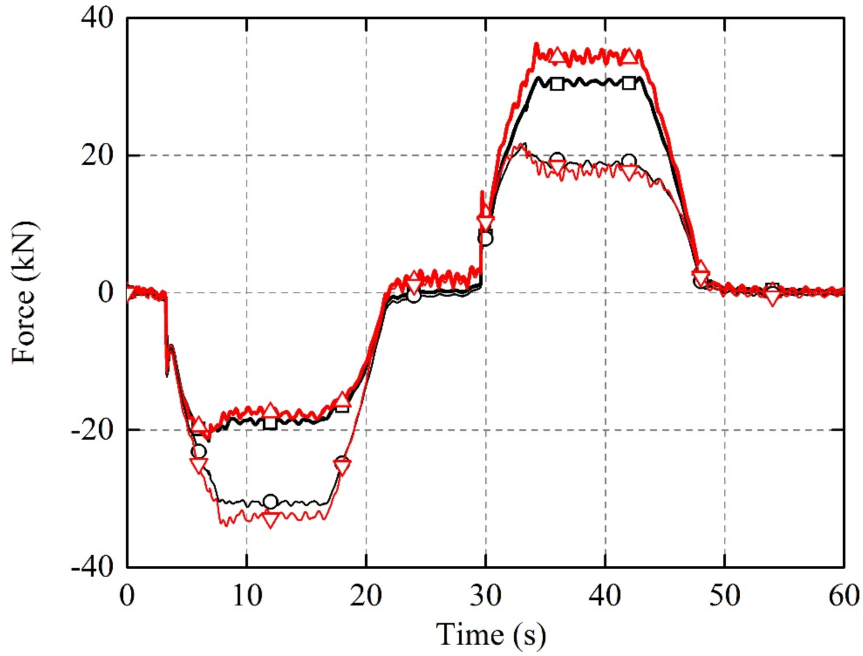

40
20
0
-20
-40
Force (kN)
0
10
20
30
40
50
60
Time (s)

(a)

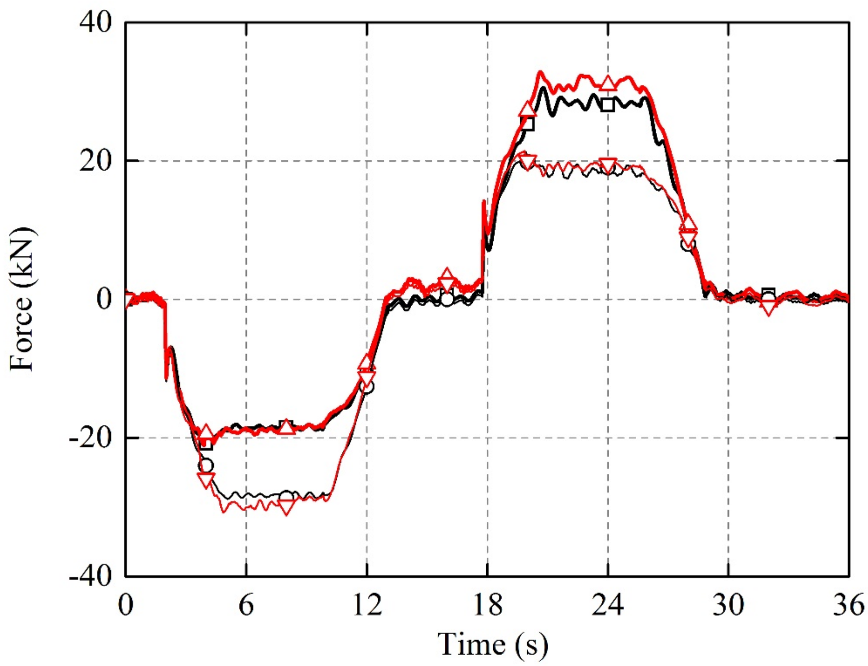

40
20
0
-20
-40
Force (kN)
0
6
12
18
24
30
36
Time (s)

(b)

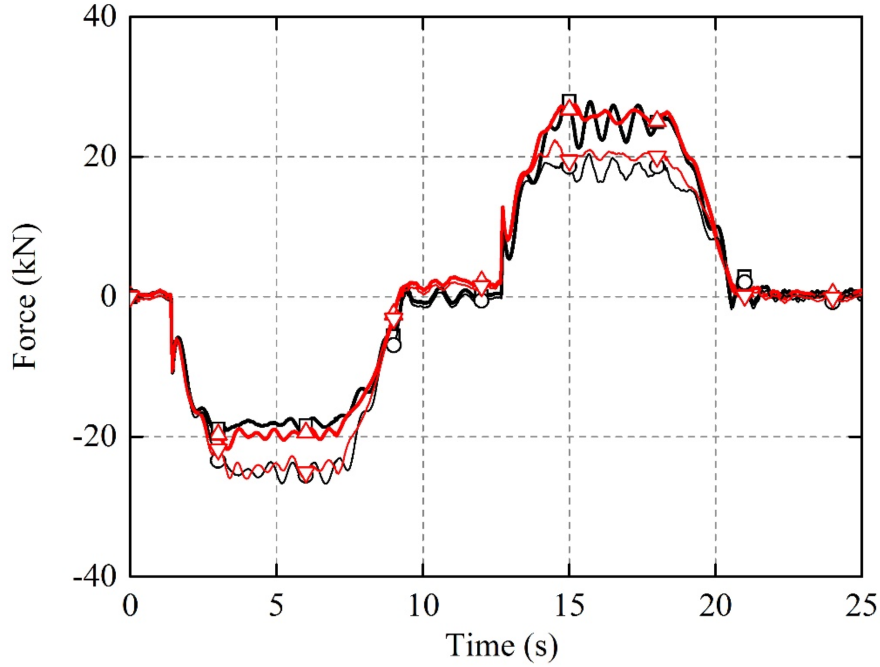

(c)

Figure 17. Tread lateral contact force of lead wheelset of lead truck. (a) 40km/h, (b) 60 km/h, (c) 90 km/h. (Rigid-Right, Fluid-Right, Rigid-Left, Fluid-Left)

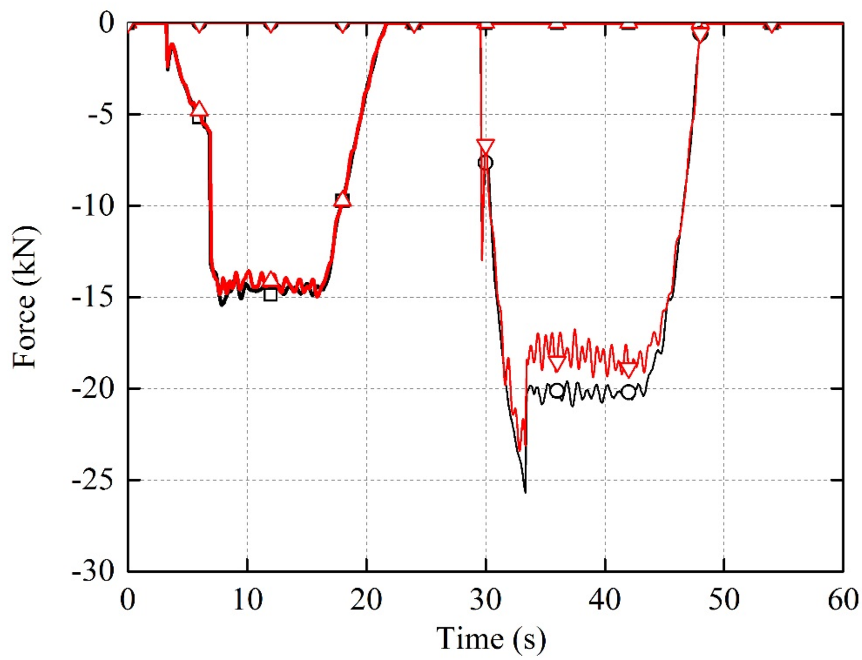

(a)

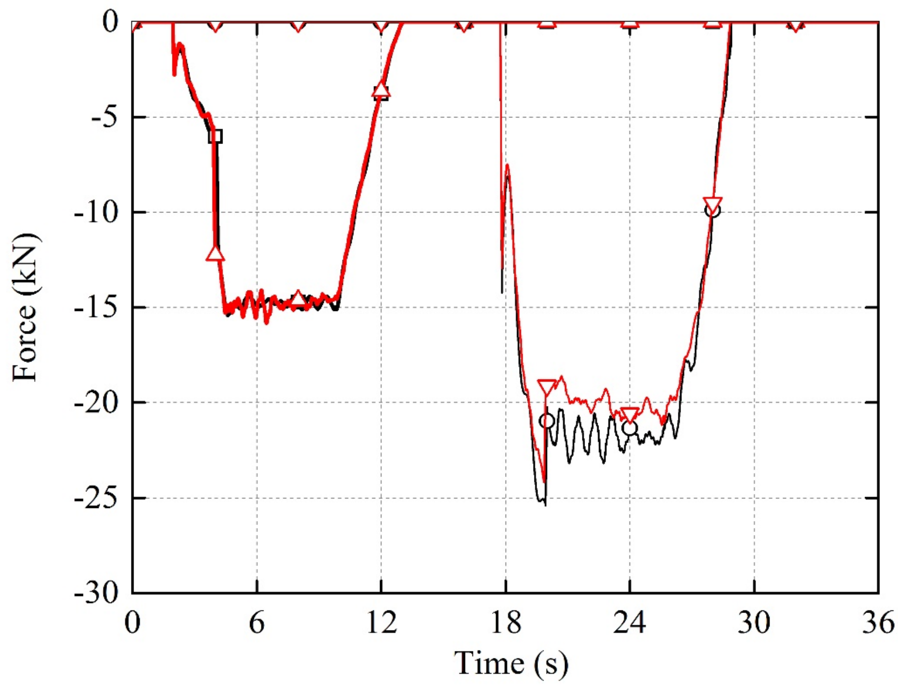

(b)

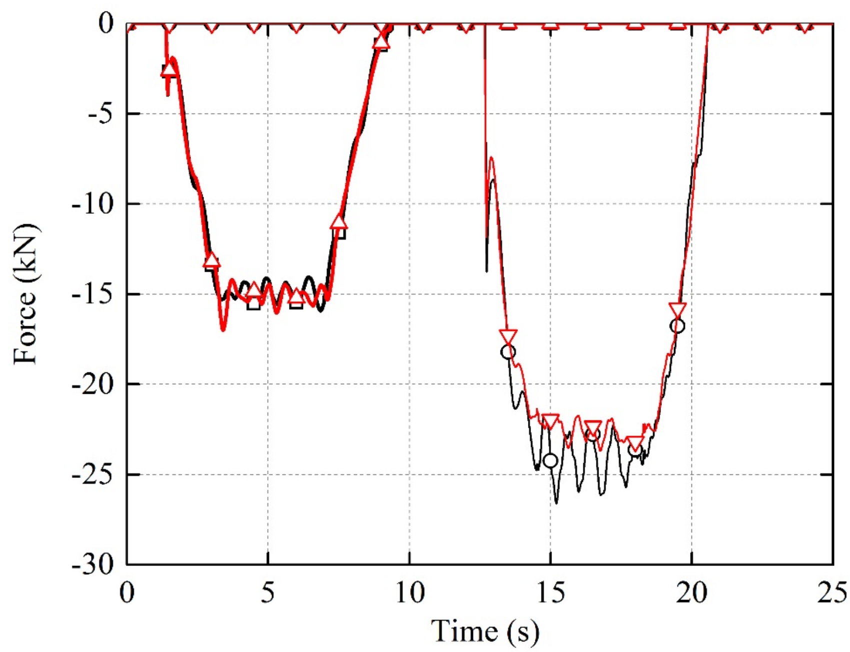

(c)

Figure 18. Flange lateral contact force of lead wheelset of lead truck. (a) 40km/h, (b) 60 km/h, (c) 90 km/h. (Rigid-Right, Fluid-Right, Rigid-Left, Fluid-Left)

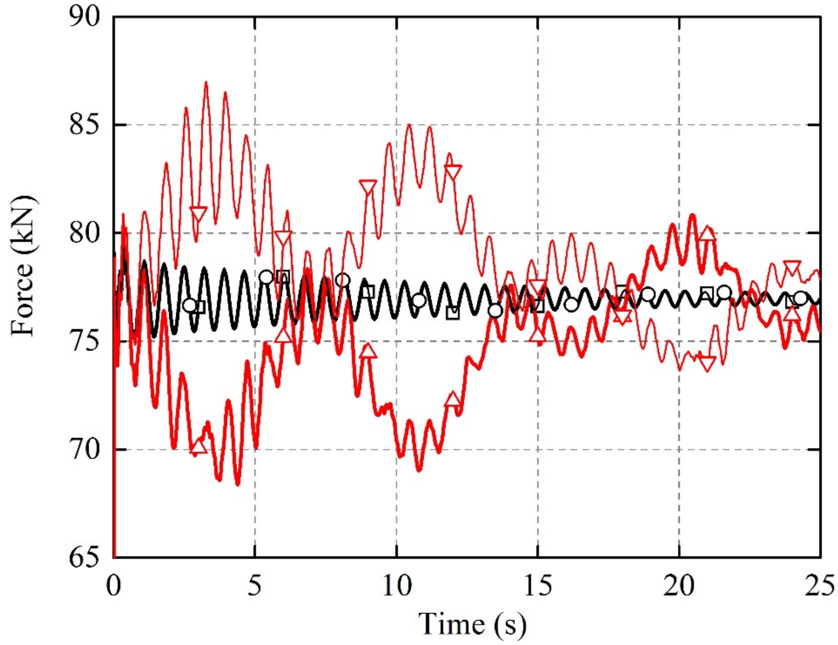

Figure 19. Average normal contact forces of lead and rear trucks in the traction case. (Rigid-Lead, Fluid-Lead, Rigid-Rear, Fluid-Rear)

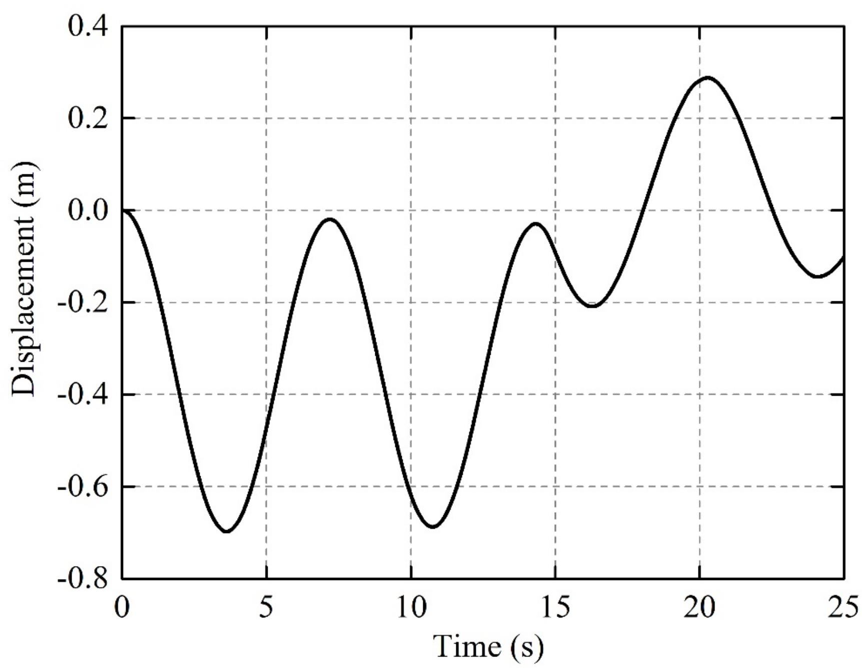

Figure 20. Fluid center of mass longitudinal displacement with respect to the tank in the traction case.

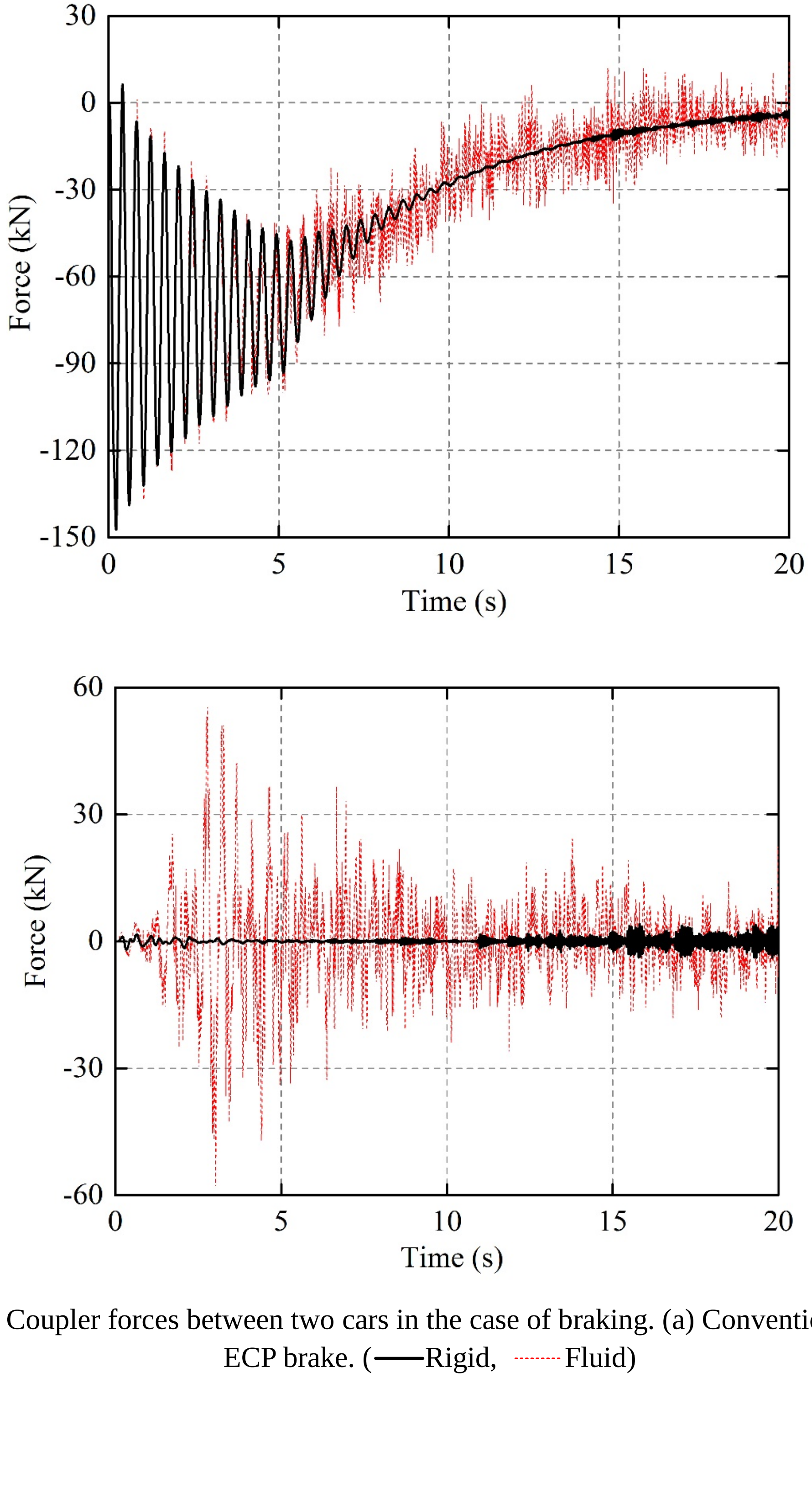

(a)

(b)

Figure 21. Coupler forces between two cars in the case of braking. (a) Conventional brake, (b) ECP brake. (——Rigid, ------- Fluid)

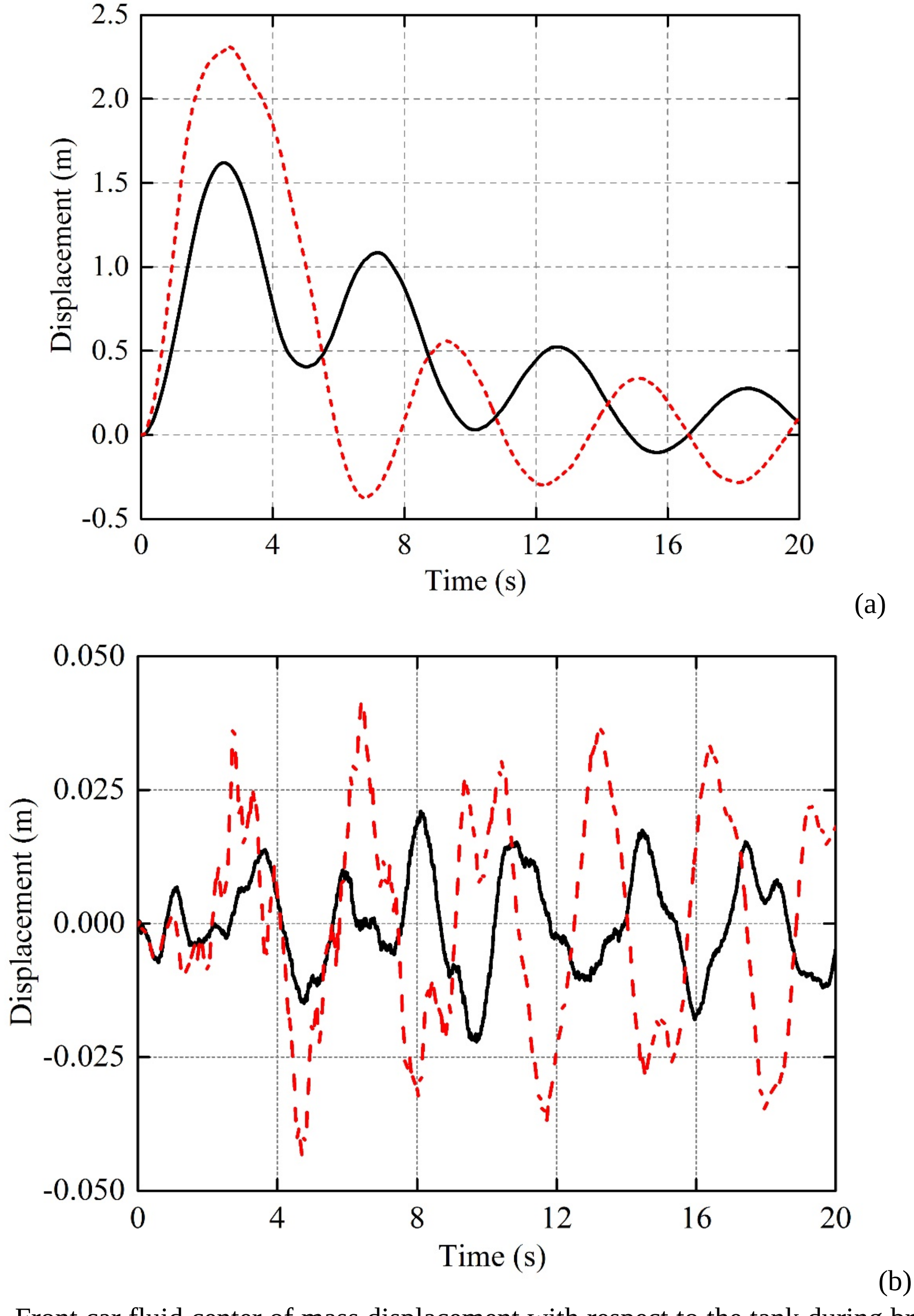

Figure 22. Front car fluid center of mass displacement with respect to the tank during braking. (a) Longitudinal, (b) Lateral direction. (——Conventional brake, ········ ECP brake)

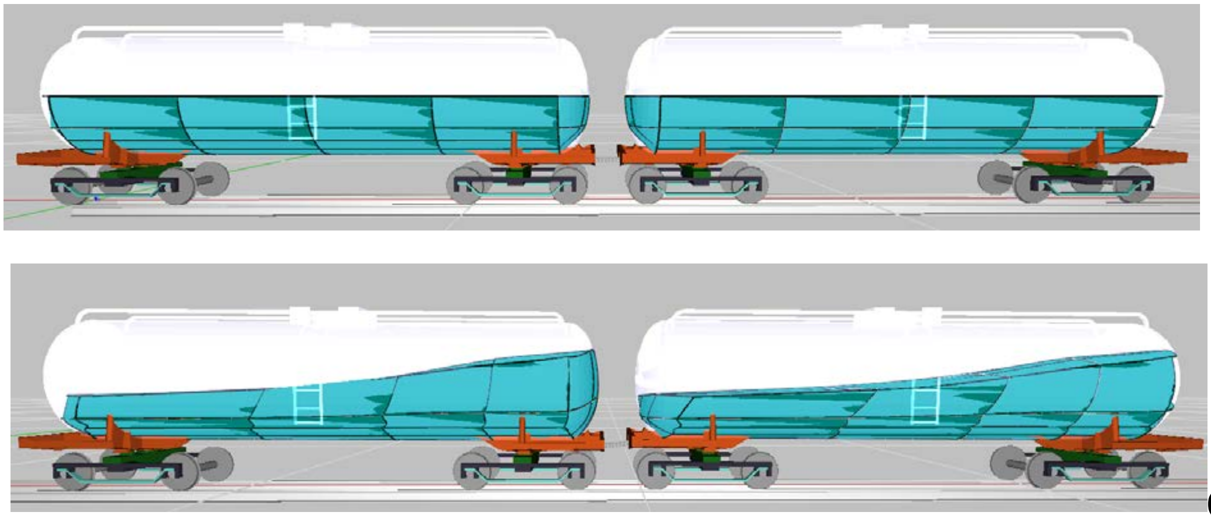
(a)
(b)

Figure 23. Braking animation of two tank-cars filled with liquid. (a) Parked state, (b) Braking state.